The architecture of an intrusion in magmatic mush

Alexandre Carrara[1*], Alain Burgisser[1], George W. Bergantz[2]

[1] Univ. Grenoble Alpes, Univ. Savoie Mont Blanc, CNRS, IRD, IFSTTAR, ISTerre, 38000 Grenoble, France.

[2] Department of Earth and Space Sciences, Box 351310, University of Washington, Seattle, WA 98195, USA

Abstract: 305 words, Main text: 5239 words, 6 Figures, 3 Tables, 50 references.

* Corresponding author: Email: carrara.alexandre.univ@gmail.com

Abstract:

Magmatic reservoirs located in the upper crust have been shown to result from the repeated intrusions of new magmas, and spend much of the time as a crystal-rich mush. The geometry of the intrusion of new magmas may greatly affect the thermal and compositional evolution of the reservoir. Despite advances in our understanding of the physical processes that may occur in a magmatic reservoir, the resulting architecture of the composite system remains poorly constrained. Here we performed numerical simulations using a computational fluid dynamics and discrete element method in order to illuminate the geometry and emplacement dynamics of a new intrusion into mush and the relevant physical parameters controlling it. Our results show that the geometry of the intrusion is to first order controlled by the density contrast that exists between the melt phases of the intrusion and resident mush rather than the bulk density contrast as is usually assumed. When the intruded melt is denser than the host melt, the intrusion pounds at the base of the mush and emplaced as a horizontal layer. The occurrence of Rayleigh-Taylor instability leading to the rapid ascent of the intruded material through the mush was observed when the intruded melt was lighter than the host one and was also unrelated to the bulk density contrast as considered before. In the absence of density contrasts between the two melt phases, the intrusion may fluidize the host crystal network and slowly ascend through the mush. The effect of the viscosity contrast between the intruded and host materials was found to have a lesser importance on the architecture of intrusions in a mush. Analyzing the eruptive sequence of well documented eruptions involving an intrusion as the trigger shows a good agreement with our modeling results, highlighting the importance of specifically considering granular dynamics when evaluating magmas and mush physical processes.

Keywords: Mush, Magma, Intrusion, Density contrast, CDF-DEM, Granular mechanics.

Introduction:

Evidence for injections of new magmas, also called recharge events, are ubiquitous in magmatic systems (Wiebe, 2016). They are inferred to cause the formation of long-lived, supersolidus magmatic reservoirs located in the upper crust (e.g. Annen et al., 2015, 2006; Dufek and Bergantz, 2005; Karakas et al., 2017). Together with the thermal structure of the upper crust and the frequency of recharge, the geometry and mode of emplacement of the intruded magma was also identified as having a crucial effect on the long-term evolution of igneous bodies (Annen et al., 2015). Diverse evidence supports the view that magmatic reservoirs reside most time in a mush state that is frequently disturbed by injection of new magmas (e.g. Bachmann and Huber, 2016; Cashman et al., 2017, and reference therein). A magmatic mush is a crystal-rich magma in which crystals are in close and sometimes frictional contacts, forming a semi-rigid framework where stress is transmitted by force chains (Bergantz et al., 2017). As a result, mushes transition between crystal-rich suspensions to a 'lock-up' state that inhibits the ability of the magma to erupt.

The injection of hotter magma into a cooler host has been suggested as a means to trigger volcanic eruptions (e.g. Caricchi et al., 2014) and the intrusion style plays a fundamental role in the way mush rejuvenates (process of recycling the mush to generate an eruptible magma) prior to eruption (Parmigiani et al., 2014, and references therein). Several scenarios assume that the intruder is emplaced as sills at the base of the mush, and rejuvenate it by supplying heat but no mass except possibly exsolved volatiles (Bachmann and Bergantz, 2006; Bergantz, 1989; Burgisser and Bergantz, 2011; Couch et al., 2001; Huber et al., 2011). Other scenarios consider that the injected magma may penetrate the mush, producing various degrees of mixing with the resident mush depending on its buoyant acceleration (e.g. Bergantz and Breidenthal, 2001; Koyaguchi and Kaneko, 2000; Weinberg and Leitch, 1998). Whether an intrusion generates extensive mass transfer, or is limited to thermal exchanges between an underplated intruder and a host mush is thus a key element shaping the outcome of open-system events. A major obstacle to our current understanding of the formation and evolution of igneous bodies is that little is known about the architecture of intrusions and controlling physical parameters.

Traditionally, mush rejuvenation scenarios have been based on the results of experiments performed with pure fluids mimicking the bulk physical properties (density and viscosity) of the magmas (e.g. Huppert et al., 1986; Jellinek and Kerr, 1999; Snyder and Tait, 1995). Mush dynamics, however, differs from that of pure fluids because of the complex rheological feedbacks between melt and crystals. An essential physical process is that melt and crystals may experience relative motions. Numerical simulations explicitly accounting for such decoupled motions as well as the building and destruction of force chains between crystals (Bergantz et al., 2015; Schleicher et al., 2016; Schleicher and Bergantz, 2017) have revealed that the local injection of pure melt of the same density and viscosity as the mush interstitial melt easily fluidizes, penetrates, and partially mixes with the overlying mush if it is sufficiently vigorous. This local unlocking of a mush suggests that the conditions of efficient mass transfer and mixing are easier to achieve than previously thought. Conversely, it is adding constraints on rejuvenation scenarios based on the emplacement of an underlying mafic gravity current (e.g. Bachmann and Bergantz, 2006; Burgisser and Bergantz, 2011) by suggesting that underplating may require contrasts in densities and/or viscosities to hinder fluidization.

Our capacity to interpret the various natural expressions of open-system events, such as eruptive products containing both the intruded magma and the resident mush, is hindered by our partial understanding of the architectural end-members of these events, such as fluidization or underplating.To characterize the geometry and emplacement styles of intrusion events into a residing mush, we performed numerical simulations using a combination of fluid mechanics and discrete elements (Bergantz et al., 2015; Schleicher et al., 2016; Schleicher and Bergantz, 2017) . As the dissimilarities between the density and viscosity of the two melts require special attention to better characterize the end-member cases of open-system events, we explored how these parameters condition the dynamics of the intruded material when injected into a mush. We first introduce the numerical model and the dimensionless parameters controlling recharge dynamics that are varied in the simulations. Results of numerical simulations involving magmas of contrasted physical properties are then presented in the framework of the dimensionless parameters. Finally, we relate our results to well-documented cases of eruptions triggered by an intrusion event.

2: Method

In order to characterize the geometry and emplacement mechanism of intrusion in mush accounting for granular dynamics, we performed Computational-Fluid-Dynamic and Discrete-Element-Method (CFD-DEM) numerical simulations by using the MFIX-DEM software (https://mfix.netl.doe.gov/). Details about the theory and implementation of the model can be found in Garg et al. (2012), Syamlal (1998), Syamlal et al. (1993), and validation of the DEM approaches in Garg et al. (2012) and Li et al. (2012) (see supplementary information 1 for a list of the equations we used). To ensure stability and efficiency of the simulations, we used the composite implicit force, which includes gravitational, pressure and drag forces, proposed by Burgisser et al. (in review) instead of the usual numerical forces evaluations (Garg et al., 2012). The composite force expression do not requires the use of time steps shorter than the characteristic durations of the hydrodynamic processes accounted. As a result, the viscosity of the melt phases may be increased without decreasing the simulation time step compared to that required to ensure the stability of a dry (zero viscosity) granular simulations.

The computational domain is a 3D medium of 1.6 × 0.8 × 0.05 m (length × height × width) filled with a resident mush (Fig. 1). This geometry also allowed us to populate the mush with mm-size particles, thereby ensuring a 1:1 scale compared to nature. We will show a posteriori that our particle bed behaves identically to a bed twice as thick (Bergantz et al., 2015). Our runs are thus representative of an open system event despite the small size of the domain compared to a natural system We used such geometry instead of a two dimensional one to ensure that the build-up and breaking of force chains have a sufficient degree of freedom in space to replicate best the mechanics of the granular phase. We created a mush layer of ~0.3 m height with an initial crystal content of ~0.64 by simulating the settling of the particles in a vacuum and positioning them at the base of the domain. We used the same density for all particles ($\rho_p = 3300$ kg m^{-3}) and three different diameters (4.5, 5, and 5.5 mm) to avoid artificial clustering. All simulations use the same initial particle bed. A crystal-free magma is injected at the base of the mush layer with a superficial vertical velocity, U_{inj}, through an inlet having a width, W_{inj}. The density and the viscosity of the injected melt are kept constant between all the simulations (

$\rho_i = 2500$ kg m^{-3}; $\eta_i = 1$ Pa s, see table 2 for the list of the parameters kept constant). We used a conduit of 3.2 cm in height to supply the inlet to ensure that the intruder enters the mush as a Poiseuille flow. At the top of the domain, we used a pressure outflow boundary conditions to ensure the overall mass conservation within the entire domain, which is consistent with an open-system event. The boundary conditions at the front and back of the domain are cyclical, which means that the intruder corresponds to a dyke having one infinite dimension. All the other boundary conditions are non-slip walls (Fig 1). To maintain constant values of melt density and viscosity during the runs (and hence constant density and viscosity contrasts), thermal effects are ignored. This is consistent with the small dimensions of the computational domain that ensure run times shorter than those allowing significant heat exchanges.

We performed simulations by varying the density and viscosity of the host melt. In order to compare simulations, we used dimensionless quantities to scale the effects of the contrasts in densities and viscosities, and injection velocities. The injection velocity and melt viscosity control the stress applied by the input of new materials to the mush. These parameters enter the minimum fluidization velocity, U_{mf} (Schleicher et al., 2016, see supplementary information 2 for derivation of U_{mf}), which expresses the minimum superficial velocity required for the injection to entrain the host solids and generate the fluidization of the particle bed. As the injected melt differs from the host melt, two minimum fluidization velocities can be calculated depending on which melt is considered. For all simulations, we used the minimum of these two velocities, which here always corresponds to that using the host melt properties. The dimensionless injection velocity, U^*, is defined as:

$$U^{*} = \frac{U_{inj}}{U_{mf}}. \tag{1}$$

In simulations having identical U^{*}, the injection imposes the same stress to the overlying mush. However, the time needed to inject the same new melt volume changes between simulations because U_{mf} varies. We thus used a dimensionless time, t^{*}, to scale the simulation time (Bergantz et al., 2017):

$$t^{*} = \frac{t\,U_{inj}}{H_{bed}}, \tag{2}$$

where t is the simulation time. In this way, simulations having identical t^{*} implies that the same volumes of intruder have been injected until that dimensionless time and simulation results can be compared directly. The density contrast between the two materials is scaled using the reduced buoyancy of the intruder. A negative reduced buoyancy indicates that the intruder is buoyant compared to the mush, whereas a positive one indicates a tendency to sink. Two reduced buoyancies may be defined. The first one, ρ^{*}, expresses the buoyancy contrast between the two melts:

$$\rho^{*} = \frac{\rho_i - \rho_h}{\rho_i}, \tag{3}$$

where ρ_i is the density of the intruded melt, and ρ_h is the host melt density. The second one, ρ_b^{*}, takes the presence of crystals in the host material into account and scales the bulk densities:

$$\rho_b^{*} = \frac{\rho_i - \left(\rho_h\left(1 - \Phi\right) + \rho_p \Phi\right)}{\rho_i}, \tag{4}$$

where ρ_p is the density of the host solids, and Φ is the particle volume fraction. The viscosity contrast, η^*, between the two melts is expressed as:

$$\eta^* = \frac{\eta_h}{\eta_i}, \tag{5}$$

where η_h is the host dynamic viscosity and η_i is that of the injected melt.

3: Results

We performed 25 numerical simulations to explore the influence of the host melt density and viscosity (See Table 3 for a list of all the simulations and corresponding parameters). For these simulations, the injection velocities are such that the ratio with the respective minimum fluidization velocity, U^*, remains constant at U^*=21.2. This ratio is chosen to match that used previously in similar works (Schleicher et al., 2016; Schleicher and Bergantz, 2017) according to the formula presented in the supplementary material 2. We performed an additional 4 simulations at higher injection velocities to explore the effect of U^* on intrusion dynamics.

Figure 2 plots the simulations at the lowest U^*, 21.2, as functions of the dimensionless quantities ρ^*, ρ_b^*, and η^*. It shows that the intrusions can be classified in three regimes as a function of the reduced buoyancy between the two melts, ρ^*. When $\rho_i = \rho_h$, the *fluidization* regime is observed. If $\rho_i > \rho_h$, the *spreading* regime occurs, whereas if $\rho_i < \rho_h$, the *rising* regime occurs (see next paragraph for a detailed description of the regime dynamics). The bulk density contrast ρ_b^* is always negative and the regime transition occurs at a value (-0.2025) of no particular physical significance. The three regimes do no depend on the viscosity contrast η^*.

The *fluidization* regime was observed in the simulations once $\rho_i = \rho_h$, and consists in the development of a fluidized area above the inlet in which the intruded melt rises through the mush (Fig. 3A–C), as described previously (Bergantz et al., 2015; Schleicher et al., 2016). The fluidization of the mush is initiated by the dilation of the crystal framework to crystal volume fraction below 0.3 above the inlet that locally destabilizes the forces chains network that supports the bed and separates the crystals in contact. The fluidized volume grows vertically above the inlet because of two mechanisms. The first is the upward entrainment of the particles localized above the fluidized cavity, which results in bulging the top surface of the mush layer (Fig. 3A–C). The second mechanism is the progressive erosion of the crystals jammed at the boundary between the mush and the fluidized volume. Once separated, crystals start settling in the fluidized area because of this process of mush erosion, causing the fluidized area to ascend faster than the intruded melt (green outline in Fig 3A–C). The intruder flows mainly vertically with a minor lateral porous flow. When the fluidized cavity reaches the top of the particle bed, its width progressively decreases to stabilize in the shape of a vertical chimney. At steady state, when $t^*>1$, the crystals located within the chimney show both upward and downward motions whereas the ones located around the chimney flow slowly in the direction of the inlet, forming a ‘mixing bowl’ as a whole, fully recovering the dynamics first described in Bergantz et al. (2015).

The *spreading* regime, which prevails in simulations once $\rho_i > \rho_h$, is characterized by the lateral spreading of the injected melt similarly to a gravity current hugging the floor of the host reservoir (Fig. 3D–F). The main difference with a pure fluid gravity current is that the melt is progressively flowing across the mush as permeable flow. At the start of the injection, the crystal framework experienced a dilation, which initiates host crystals settling in the same fashion as in the *fluidization* regime. The lateral flow of the intruded melt is able to laterally entrain the host crystals, creating two counter rotating granular vortexes in the residing mush with downward motions above the inlet (Fig. 3D–F). Such granular vorticity affects the flow pattern of the fluid in the mush. The fluidized volume grows either predominantly laterally or vertically, depending on the relative importance between the lateral entrainment of the host solids by the intruder and the vertical settling of the mush crystals. As the lateral propagation of the intruder progresses, so does the size of the two granular vortexes, making this style of intrusion affect a larger mush volume than the *fluidization* regime.

The *rising* regime (Fig. 3G–I), is characterized by the ascent of the intruded melt within the mush that occurred in simulations once $\rho_i < \rho_h$. Runs start with the initial growth above the inlet of a cavity filled with the intruded fluid. The cavity becomes gravitationally unstable and ascends within the mush, forming a Rayleigh-Taylor instability. The ascent of the intruder continues above the particle bed, entraining solids from the host. The instability is driven by its head because of the buoyant batch of intruded melt. This driving batch is surrounded by a volume of fluidized host mush (Fig. 3G–I). The dimensionless time at which the intrusion reaches the mush top (t^*~0.3) is shorter than that of the two other regimes because the Rayleigh-Taylor instability significantly accelerates the transport of the intruder.

Figure 2 suggests that the viscosity contrast does not control the end-member shape of the intruder flow. Larger viscosity contrasts, however, increase the trends of some aspects of mush dynamics. Figure 3 illustrates how viscosity bears on flow patterns.

In the *fluidization* regime, the increase of the host viscosity enhances the formation of crystal-poor batches at the top of the intruded volume (Fig. 3A–C). Because the minimum fluidization velocity within the intruded melt is lower than for the host, the crystals are not fluidized and sediment in the intruded melt to accumulate atop the inlet (Fig 3B–C). Because we defined t^* to scale the dynamics of the mush, the increase of the host melt viscosity decreases the injection velocity and the duration, t, required to reach the dimensionless time $t^*=1$. As a result, increasing melt viscosity increases the ability for the intruded melt to experience lateral porous flow through the host crystal frameworks (Fig. 3B–C). It also lengthens the time span for a crystal to settle over the same characteristic distance between the intruded and host melts, which results in the formation of the crystal poor volume at the top of the intruded volume (Fig. 3B–C). The increase in the host melt viscosity, however, does not affect the volume of mush showing a decrease in crystal volume faction and a distortion of the force chains.

In the *spreading* regime, high viscosity contrasts enhance the lateral spreading of the intruder and the entrainment of the host crystals in the two counter rotating vortexes (Fig 3E–F). Large host melt viscosity causes the lateral entrainment of the solids to be more efficient than particle settling, which results in the elongation of the fluidized volume in the horizontal direction. In the same fashion as in the *fluidization* regime, the lower superficial injection rate enhances the ability of the lateral porous flow of the intruder. This effect is expressed by the decrease of the thickness of the intruded layer with the increase of the host viscosity (Fig 3D–F).

It results that reaching the same volume of mush entrained by the intrusion requires less intruded material as the viscosity of the host melt increases.

In the *rising* regime, increasing the viscosity contrast enlarges the vortexes sizes and the separation distance between their centers (Fig 3G−I). The dimensionless time, t^*, at which the intruder instability occurs decreases with the viscosity of the host. The volume of the intruded melt driving the Rayleigh-Taylor instabilities is lower when a viscosity contrast exists. When a viscosity contrast is present, the volume of the intruded driving the instability does not vary significantly (Fig 3H−I). The larger volume of the intruder driving the Rayleigh-Taylor instability can be addressed by the ratio between the dimensional injection rate and Rayleigh-Taylor growing rate. In Fig. 3G, this ratio is higher than in Fig 3H–I, and a significant volume of fluid is injected during the growth and entrainment of the instability. On the contrary, in Fig 3H–I, this ratio is sufficiently small so that the amount of melt injected during the growth of the instability is negligible compared to the volume required to initiate it. However, the volume of the mush remobilized by the intruder flow does not significantly vary with the host melt viscosity (Fig. 3G−I).

The additional 4 simulations in the spreading regime suggest that buoyancy effects dominate the intruder flow up to $U^* \simeq 10^5$. Figure 4 shows the temporal evolution of the height reached by the intruded volume, H^*, as a function of injection rate. All injections grow purely vertically at first ($t^* \leq 0.1$). As seen above, at the low injection rate of 21.2, the intrusion stalls rapidly and spreads laterally (simulation A25, Fig. 4). Increasing the injection rate causes stalling to occur later and higher. When $t^* > 0.2$, injection growth switches from vertical to radial. When

$U^{*}>10^{5}$, the behavior of the intruder is dominated by the injection rate, which causes the radially growing intrusion to reach the top of the bed at $H^{*}=1$. Despite that all simulations have the same intruder shape before stalling, the size of the region surrounding the intruder that is affected by dilatancy increases with U^{*}. The highest injection rate (simulation B4 with $U^{*}=10^{6}$) strictly follows the theoretical curve for a radial growth and reaches $H^{*}=1$ at $t^{*}\approx 2.5$, as predicted by geometrical arguments (supplementary information 3).

The decoupling between the motions of the two phases results from processes unique to granular mechanics that our discrete numerical model is able to capture. Mush dilation is key for permeable melt flow to occur. The initiation of the intrusion increases the pore pressure in the mush around the inlet (Fig. 5A). This overpressure progressively propagates outwards and decreases the crystal volume fraction in the overlying mush (Fig. 5B). As the intrusion propagates, the effect of the overpressure is supplemented with the Reynolds dilatancy generated by the granular vortexes in the mush (Fig 5C). The dilation of the solid framework increases its permeability of the solid framework and in turn the possibility of relative motion between the crystals and the interstitial melt (Fig. 5C). This phenomenon is particularly clear in the case of the rising regime. The intruder is surrounded by a volume of mush that underwent such dilation that it is in the dilute regime. The contact region between the two magmas is dominated by melt–melt interface interspersed with isolated crystals. As a result, entrainment is ruled by melt vorticity. Efficient entrainment of two fluids with a viscosity contrast occurs only when the most viscous fluid bears large levels of vorticity (Jellinek and Kerr, 1999). In our runs, the intruder melt viscosity is equal or less than that of the host, and the vorticity is concentrated close to or inside the intrusion (Fig. S4 in the supplementary information 4). This situation yields the weak entrainment observed in the rising regime and the transition from vertical growth to spreading of the intrusion melt as injection velocity decreases (Fig. 4). The concept of bulk reduced buoyancy thus fails to predict the intrusion geometry for two reasons. First, it assumes the absence of relative motion and thus ignores the transfer of crystals from host to intrusion. Second, in cases when sufficient mush dilation occurs, entrainment is controlled by the melt–melt interface and the associated density and viscosity contrasts. The interplay between pore pressure, dilation, melt interface dynamics, and permeable flow controls the transport of mass within our modeled magmatic reservoir.

4: Comparison with natural systems

To test the applicability of our results to natural cases, we gathered from the literature the physical parameters of 15 eruptions involving the intrusion of new magma (Table S3–S4 in the supplementary information 5). All host magmas are mushes but for a few cases that either have crystal gradients in their reservoirs (Krakatau), or for which there is ambiguity on the respective roles of the intruder and host magmas (Unzen, Minoan, and Katmai–Novarupta). In the studies surveyed, melt viscosity and melt density of host magmas were most often directly determined from eruptive products and pre-eruptive conditions such as pressure, temperature, and melt water content (details on how parameters were obtained are in Table S3–S4 (see supplementary information 5)).

The cases are organized into three categories depending on the observed eruptive sequence. In the first category, the intruder was erupted first, followed by the emission of host magma or a mixture of host and intruder. This category implies that the intruder magma was able to efficiently penetrate and pass through the host magma. In the second category, both host and intruder magmas were erupted simultaneously, with the intruder most often forming enclaves or mingling structures. The last category feature cases where the mixing was so thorough that the eruptive products only bear cryptic traces of the intruder, such as isolated intruder crystals floating in the host or crystal disequilibrium textures.

Figure 6A shows the ratios of bulk viscosities and bulk densities between the intruder magma and the host magma(s) for the 15 eruptions. Figure 6A contains two physically meaningful thresholds, that of neutral buoyancy at the bulk density ratio of 0 and that of equal viscosity at the bulk viscosity ratio of one. The three types of eruptive sequence are not sorted following any of these thresholds. Figure 6B shows the same eruptions plotted as functions of melt properties instead of bulk properties. Our numerical runs cover the full range of natural density ratios and a more restricted range of viscosity ratios (from 1 to 10^2 vs. 10^{-1} to $<10^4$ in nature). Figure 6B also shows the dividing line between rising and spreading dynamics at the level of neutral buoyancy with respect to the melts. With the possible exception of two cases (see *Discussion*), the Minoan eruption and the 1912 Katmai–Novarupta eruption, the *rising* regime is populated by the eruptions that first ejected intruder material. This divide between cases where at least some of the intruder magma had the capacity to go unscathed through the host and cases where none of it escaped from host interaction is consistent with our numerical results.

5: Discussion

Our results are helpful to predict the behavior of an intrusion within a mush. The reduced buoyancy between the two melts, ρ^*, is the parameters having a first order control on the geometry of the intrusion. On the contrary, the commonly used level of neutral bulk buoyancy (e.g. Huppert et al., 1986; Snyder and Tait, 1995) does not mark any particular change in dynamic behavior (Fig. 2). This result illustrates that the relative motion between the solids and surrounding melt is of primary importance when studying mush processes. Experiments, or numerical simulations, that account of the presence of the solids or exsolved volatiles as discrete entities (Barth et al., 2019; Bergantz et al., 2015; Girard and Stix, 2009; Hodge et al., 2012; McIntire et al., 2019; Michioka and Sumita, 2005; Parmigiani et al., 2014; Schleicher et al., 2016; Schleicher and Bergantz, 2017) are the most likely to faithfully reproduce mush dynamics. Neglecting phase decoupling by considering the magma as a single-phase fluid having effective properties such as bulk density or bulk viscosity will not capture the blending of crystal contents between host and intruder and the simultaneous but independent evolution of the melt–melt interface (Fig. 5C). This sheds light on the importance of granular mechanisms such as pore pressure, dilatancy and permeable flow in shaping the end-member cases of mush intrusion.

We characterized the parameter ranges of a series of well-documented cases of eruptions that features magma mixing, focusing on the densities and viscosities of the two end-member magmas involved and on the order of the eruptive sequence. Two cases, Katmai and the Minoan eruption, straddle two eruptive sequence categories because the intruders may have been transported alongside (as opposed to through) the host magmas. Both cases are close to the neutral buoyancy level, regardless of the scenario considered (Fig. 6B). Importantly, each individual scenario is consistent with our regimes. The Katmai eruption first emitted rhyolite. The Katmai scenario corresponding to a rhyolite intruding a more mafic host (Eichelberger and Izbekov, 2000) is consistent with it being located in the *rising* regime. In the other scenario

(Singer et al., 2016), the rhyolite is part of the host reservoir, which is consistent with that scenario being in the spreading regime. The Minoan scenario located in the rising regime (Cadoux et al., 2014) would have indeed emitted the intruder first, but it feature a host filled by low-crystallinity magma, which is at odds with our hypothesis that the host is in a mush state. The other Minoan scenario (Druitt, 2014; Flaherty et al., 2018; Martin et al., 2010) involves a mushy host compatible with this hypothesis and is consistent with the spreading regime that hinders first emission of the intruder. The overall good agreement between the observed eruptive sequences and our numerical results (Fig. 6B) constitutes a serious argument in favor of the fact that open-system events are, to first order, controlled by the density contrast between the melt phases of the intrusion and mush. It also suggests that injection momentum was quickly exhausted, letting buoyancy control the unfolding of the event.

Two special natural cases can be added to the comparison between our dynamics regime and natural data (Fig. 6B). The first is the 1883 eruption of Krakatau volcano (Mandeville et al., 1996), which resulted from remobilization by basaltic intruder of a stratified magma chamber featuring three compositions, none of them being in a mush state (andesite, dacite, and rhyodacite). Evidence that the basalt intruder was erupted first comes from basaltic ashes collected during the first phase of the eruption (Self, 1992). The presence of several magmas in the host reservoir, however spatially distributed, causes a large uncertainty in the host properties. As a result, the Krakatau eruption spans the divide between the regimes established by our simulations (Fig. 6B). It is thus an inconclusive case where the intruder was erupted first. The second natural case is the 1991–1995 eruption of Unzen volcano, for which the intruder could have been either andesitic (Holtz et al., 2004), or basaltic (Browne et al., 2006). Regardless of its composition, the intrusion caused thorough mixing and the first magma erupted was the product of this mixing. If the intruder was basaltic, it was buoyant with respect to the felsic host and if it was andesitic, it was denser that the host. As a result, Unzen spans the divide between the *rising* and *spreading* regime (Fig. 6B). Considering that the intruder input was large (>30 wt% of the eruptive products; Holtz et al., 2005), and if any credit is given to our inferences, the intruder was more likely to be andesitic than basaltic because this latter composition would have been prone to preserve its integrity while going through the host mush, erupting first.

6: Conclusions

This study highlights the importance of granular mechanics in mush processes, which differ significantly from ones expected with purely fluid models. As expected, our simulations show that when the injection velocity is high ($U^*>10^5$), intrusion dynamics is dominated by the injection momentum and the intruded cavities grow radially. When the injection velocity is below this threshold, however, buoyancy controls the behavior of the intruder in an unexpected way. Bulk buoyancy contrasts appear to play no role in the way the intruder flows. Instead, the density contrast between the host and intruded melts exerts a first-order control on the architecture of an intrusion event in a mush. When the two melt densities are identical, the intruder fluidizes the mush and creates a mixing bowl, as described in Bergantz et al. (2015). When the intruded melt is lighter than that of the host, it rises through the mush. Mush dilation around the intruder causes the contact region between the two magmas to be dominated by melt–melt interface interspersed with isolated crystals. Entrainment in this rising regime is ruled by the amount of vorticity of the most viscous melt. As our in our runs the intruder melt viscosity was equal or lower than that of the host, no entrainment was observed. Intruder melts denser than the host spread laterally partly as permeable flows through the host mush. The lateral spreading of the intruder generates two counter rotating granular vortexes with downward motions above the inlet, which maximizes the volume of the mush entrained by the gravity current. In this spreading regime, the combined effects of the initial pore overpressure at the inlet and the Reynolds dilatancy resulting from the lateral spreading of the intruder are able to fluidize the overlying mush.

We tested whether the first-order effect of melt density contrast was expressed in nature. We tallied 15 well-documented eruptive sequences, classifying them according to the expected outcomes of the three dynamic regimes we defined. We found overall good agreement between eruption sequences and our model predictions, which suggests that granular mechanisms such as pore pressure, dilatancy, and permeable flow play a fundamental role in the unfolding of open-system events. Granular dynamics and the decoupling of melt and crystals are thus key in shaping reservoir and volcanic processes.

Acknowledgments:

All the numerical simulations presented in this paper were performed using the CIMENT infrastructure (https://ciment.ujf-grenoble.fr), which is supported by the Rhône-Alpes region (GRANT CPER07_13 CIRA: http://www.ci-ra.org). G.W.B. was supported by National Science Foundation grants DGE-1256068, EAR-1049884 and EAR-1447266. Authors declare no conflicts of interest.

References:

Annen, C., Blundy, J.D., Leuthold, J., Sparks, R.S.J., 2015. Construction and evolution of igneous bodies: Towards an integrated perspective of crustal magmatism. Lithos 230, 206–221. https://doi.org/10.1016/j.lithos.2015.05.008

Annen, C., Blundy, J.D., Sparks, R.S.J., 2006. The Genesis of Intermediate and Silicic Magmas in Deep Crustal Hot Zones. J Petrology 47, 505–539. https://doi.org/10.1093/petrology/egi084

Bachmann, O., Bergantz, G.W., 2006. Gas percolation in upper-crustal silicic crystal mushes as a mechanism for upward heat advection and rejuvenation of near-solidus magma bodies. Journal of Volcanology and Geothermal Research 149, 85–102. https://doi.org/10.1016/j.jvolgeores.2005.06.002

Bachmann, O., Huber, C., 2016. Silicic magma reservoirs in the Earth's crust. American Mineralogist 101, 2377–2404. https://doi.org/10.2138/am-2016-5675

Barth, A., Edmonds, M., Woods, A., 2019. Valve-like dynamics of gas flow through a packed crystal mush and cyclic strombolian explosions. Sci Rep 9, 1–9. https://doi.org/10.1038/s41598-018-37013-8

Bergantz, G.W., 1989. Underplating and Partial Melting: Implications for Melt Generation and Extraction. Science 245, 1093–1095. https://doi.org/10.1126/science.245.4922.1093

Bergantz, G.W., Breidenthal, R.E., 2001. Non-stationary entrainment and tunneling eruptions: A dynamic link between eruption processes and magma mixing. Geophysical Research Letters 28, 3075–3078. https://doi.org/10.1029/2001GL013304

Bergantz, G.W., Schleicher, J.M., Burgisser, A., 2017. On the kinematics and dynamics of crystal-rich systems. J. Geophys. Res. Solid Earth 122, 2017JB014218. https://doi.org/10.1002/2017JB014218

Bergantz, G.W., Schleicher, J.M., Burgisser, A., 2015. Open-system dynamics and mixing in magma mushes. Nature Geosci 8, 793–796. https://doi.org/10.1038/ngeo2534

Browne, B.L., Eichelberger, J.C., Patino, L.C., Vogel, T.A., Uto, K., Hoshizumi, H., 2006. Magma mingling as indicated by texture and Sr/Ba ratios of plagioclase phenocrysts from Unzen volcano, SW Japan. Journal of Volcanology and Geothermal Research, Modern Trends in Petrography: 154, 103–116. https://doi.org/10.1016/j.jvolgeores.2005.09.022

Burgisser, A., Bergantz, G.W., 2011. A rapid mechanism to remobilize and homogenize highly crystalline magma bodies. Nature 471, 212–215. https://doi.org/10.1038/nature09799

Burgisser, A., Carrara, A., Annen, C., in review. Numerical simulations of magmatic enclave deformation. Journal of Volcanology and Geothermal Research (submitted).

Cadoux, A., Scaillet, B., Druitt, T.H., Deloule, E., 2014. Magma Storage Conditions of Large Plinian Eruptions of Santorini Volcano (Greece). J Petrology 55, 1129–1171. https://doi.org/10.1093/petrology/egu021

Caricchi, L., Annen, C., Blundy, J., Simpson, G., Pinel, V., 2014. Frequency and magnitude of volcanic eruptions controlled by magma injection and buoyancy. Nature Geoscience 7, 126–130. https://doi.org/10.1038/ngeo2041

Cashman, K.V., Sparks, R.S.J., Blundy, J.D., 2017. Vertically extensive and unstable magmatic systems: A unified view of igneous processes. Science 355, eaag3055. https://doi.org/10.1126/science.aag3055

Coombs, M.L., Gardner, J.E., 2001. Shallow-storage conditions for the rhyolite of the 1912 eruption at Novarupta, Alaska. Geology 29, 775–778. https://doi.org/10.1130/0091-7613(2001)029<0775:SSCFTR>2.0.CO;2

Couch, S., Sparks, R.S.J., Carroll, M.R., 2001. Mineral disequilibrium in lavas explained by convective self-mixing in open magma chambers. Nature 411, 1037–1039. https://doi.org/10.1038/35082540

Druitt, T.H., 2014. New insights into the initiation and venting of the Bronze-Age eruption of Santorini (Greece), from component analysis. Bull Volcanol 76, 794. https://doi.org/10.1007/s00445-014-0794-x

Dufek, J., Bergantz, G.W., 2005. Lower Crustal Magma Genesis and Preservation: a Stochastic Framework for the Evaluation of Basalt–Crust Interaction. J Petrology 46, 2167–2195. https://doi.org/10.1093/petrology/egi049

Eichelberger, J.C., Izbekov, P.E., 2000. Eruption of andesite triggered by dyke injection: contrasting cases at Karymsky Volcano, Kamchatka and Mt Katmai, Alaska. Philosophical Transactions of the Royal Society of London. Series A: Mathematical, Physical and Engineering Sciences 358, 1465–1485.

Flaherty, T., Druitt, T.H., Tuffen, H., Higgins, M.D., Costa, F., Cadoux, A., 2018. Multiple timescale constraints for high-flux magma chamber assembly prior to the Late Bronze Age eruption of Santorini (Greece). Contrib Mineral Petrol 173, 75. https://doi.org/10.1007/s00410-018-1490-1

Garg, R., Galvin, J., Li, T., Pannala, S., 2012. Open-source MFIX-DEM software for gas–solids flows: Part I—Verification studies. Powder Technology 220, 122–137.

Girard, G., Stix, J., 2009. Buoyant replenishment in silicic magma reservoirs: Experimental approach and implications for magma dynamics, crystal mush remobilization, and eruption. J. Geophys. Res. 114, B08203. https://doi.org/10.1029/2008JB005791

Hammer, J.E., Rutherford, M.J., Hildreth, W., 2002. Magma storage prior to the 1912 eruption at Novarupta, Alaska. Contributions to Mineralogy and Petrology 144, 144–162.

Hodge, K.F., Carazzo, G., Jellinek, A.M., 2012. Experimental constraints on the deformation and breakup of injected magma. Earth and Planetary Science Letters 325–326, 52–62. https://doi.org/10.1016/j.epsl.2012.01.031

Holtz, F., Sato, H., Lewis, J., Behrens, H., Nakada, S., 2004. Experimental petrology of the 1991–1995 Unzen dacite, Japan. Part I: phase relations, phase composition and pre-eruptive conditions. Journal of petrology 46, 319–337.

Huber, C., Bachmann, O., Dufek, J., 2011. Thermo-mechanical reactivation of locked crystal mushes: Melting-induced internal fracturing and assimilation processes in magmas. Earth and Planetary Science Letters 304, 443–454. https://doi.org/10.1016/j.epsl.2011.02.022

Huppert, H.E., Sparks, R.S.J., Whitehead, J.A., Hallworth, M.A., 1986. Replenishment of magma chambers by light inputs. Journal of Geophysical Research: Solid Earth 6113–6122. https://doi.org/10.1029/JB091iB06p06113@10.1002/(ISSN)2169-9356.OPENSYS1

Jellinek, A.M., Kerr, R.C., 1999. Mixing and compositional stratification produced by natural convection: 2. Applications to the differentiation of basaltic and silicic magma chambers and komatiite lava flows. Journal of Geophysical Research: Solid Earth 104, 7203–7218. https://doi.org/10.1029/1998JB900117

Karakas, O., Degruyter, W., Bachmann, O., Dufek, J., 2017. Lifetime and size of shallow magma bodies controlled by crustal-scale magmatism. Nature Geoscience 10, 446–450. https://doi.org/10.1038/ngeo2959

Koyaguchi, T., Kaneko, K., 2000. Thermal evolution of silicic magma chambers after basalt replenishments. Earth and Environmental Science Transactions of The Royal Society of Edinburgh 91, 47–60. https://doi.org/10.1017/S0263593300007288

Li, T., Garg, R., Galvin, J., Pannala, S., 2012. Open-source MFIX-DEM software for gas-solids flows: Part II—Validation studies. Powder Technology 220, 138–150.

Mandeville, C.W., Carey, S., Sigurdsson, H., 1996. Magma mixing, fractional crystallization and volatile degassing during the 1883 eruption of Krakatau volcano, Indonesia. Journal of Volcanology and Geothermal Research 74, 243–274.

Martin, V.M., Davidson, J., Morgan, D., Jerram, D.A., 2010. Using the Sr isotope compositions of feldspars and glass to distinguish magma system components and dynamics. Geology 38, 539–542. https://doi.org/10.1130/G30758.1

Mastin, L.G., 2002. Insights into volcanic conduit flow from an open-source numerical model. Geochemistry, Geophysics, Geosystems 3, 1–18. https://doi.org/10.1029/2001GC000192

McIntire, M.Z., Bergantz George W., Schleicher Jillian M., 2019. On the hydrodynamics of crystal clustering. Philosophical Transactions of the Royal Society A: Mathematical, Physical and Engineering Sciences 377, 20180015. https://doi.org/10.1098/rsta.2018.0015

Michioka, H., Sumita, 2005. Rayleigh-Taylor instability of a particle packed viscous fluid: Implications for a solidifying magma. Geophysical Research Letters 32. https://doi.org/10.1029/2004GL021827

Nakamura, M., 1995. Continuous mixing of crystal mush and replenished magma in the ongoing Unzen eruption. Geology 23, 807–810.

Pallister, J.S., Hoblitt, R.P., Meeker, G.P., Knight, R.J., Siems, D.F., 1996. Magma mixing at Mount Pinatubo: petrographic and chemical evidence from the 1991 deposits. Fire and mud: eruptions and lahars of Mount Pinatubo, Philippines 687–731.

Parmigiani, A., Huber, C., Bachmann, O., 2014. Mush microphysics and the reactivation of crystal-rich magma reservoirs. Journal of Geophysical Research: Solid Earth 119, 6308–6322. https://doi.org/10.1002/2014JB011124

Schleicher, J.M., Bergantz, G.W., 2017. The Mechanics and Temporal Evolution of an Open-system Magmatic Intrusion into a Crystal-rich Magma. J Petrology 58, 1059–1072. https://doi.org/10.1093/petrology/egx045

Schleicher, J.M., Bergantz, G.W., Breidenthal, R.E., Burgisser, A., 2016. Time scales of crystal mixing in magma mushes. Geophysical Research Letters 43, 1543–1550. https://doi.org/10.1002/2015GL067372

Self, S., 1992. Krakatau revisited: The course of events and interpretation of the 1883 eruption. GeoJournal 28, 109–121. https://doi.org/10.1007/BF00177223

Singer, B.S., Costa, F., Herrin, J.S., Hildreth, W., Fierstein, J., 2016. The timing of compositionally-zoned magma reservoirs and mafic 'priming' weeks before the 1912 Novarupta-Katmai rhyolite eruption. Earth and Planetary Science Letters 451, 125–137. https://doi.org/10.1016/j.epsl.2016.07.015

Snyder, D., Tait, S., 1995. Replenishment of magma chambers: comparison of fluid-mechanic experiments with field relations. Contrib Mineral Petrol 122, 230–240. https://doi.org/10.1007/s004100050123

Syamlal, M., 1998. MFIX documentation numerical technique. EG and G Technical Services of West Virginia, Inc., Morgantown, WV (United States).

Syamlal, M., Rogers, W., OBrien, T.J., 1993. MFIX documentation theory guide. USDOE Morgantown Energy Technology Center, WV (United States).

Tomiya, A., Takahashi, E., 1995. Reconstruction of an Evolving Magma Chamber beneath Usu Volcano since the 1663 Eruption. J Petrology 36, 617–636. https://doi.org/10.1093/petrology/36.3.617

Weinberg, R.F., Leitch, A.M., 1998. Mingling in mafic magma chambers replenished by light felsic inputs: fluid dynamical experiments. Earth and Planetary Science Letters 157, 41–56. https://doi.org/10.1016/S0012-821X(98)00025-9

Wiebe, R.A., 2016. Mafic replenishments into floored silicic magma chambers. American Mineralogist 101, 297–310. https://doi.org/10.2138/am-2016-5429

Tables:

Symbol (unit)	Definition
d_p (m)	Particle diameter
E (Pa)	Particle Young modulus
$\overrightarrow{F_{GPD}}$ (N)	Gravity-Pressure-Drag force
$\vec{g}$ (m s^{-2})	Gravity acceleration vector
H_{bed} (m)	Particle bed thickness
H_{max} (m)	Intruded layer maximum height above the inlet
H^*	Dimensionless height of the intruded volume
m_p (kg)	Particle mass
P (Pa)	Fluid pressure
R (m)	Intruder batch radius
t^*	Reduced time
U_{inj} (m s^{-1})	Injection superficial velocity
U_{mf} (m s^{-1})	Minimum fluidization superficial velocity
U^*	Dimensionless injection velocity
$\vec{v}_f$ (m s^{-1})	Fluid velocity vector
$\vec{v}_p$ (m s^{-1})	Particle velocity vector
W_{inj} (m)	Injection width
ρ_f (kg m^{-3})	Fluid density
η (Pa s)	Fluid dynamic viscosity
τ_v (s)	Particle viscous response time
β (kg s^{-1})	Momentum transfer coefficient
Δt (s)	DEM time step
η (Pa s)	Fluid dynamic viscosity
η_i (Pa s)	Intruder melt dynamic viscosity
η_h (Pa s)	Host melt dynamic viscosity
η^*	Melts dynamic viscosity ratio
μ	Particle friction coefficient
ρ_h (kg m^{-3})	Host melt density
ρ_i (kg m^{-3})	Intruder melt density
ρ_p (kg m^{-3})	Average density of the particles
ρ^*	Melts reduced buoyancy
ρ_b^*	Melts bulk reduced buoyancy
σ	Poisson coefficient
τ_v (s)	Particle viscous response time
Φ	Solid volume fraction

Table 1: List of symbols and their meaning

Parameter	Value or range
ρ_p	3300 kg m^{-3}
d_p	4.5-5.5 mm
Nb crystals	208495
H_{bed}	0.3 m
W_{inj}	0.1 m
ρ_i	2500 kg m^{-3}
η_i	1 Pa s
E	2 10^{7} Pa
σ	0.32
μ	0.3

Table 2: Parameters kept constant during the parametric study

Run nb.	ρ_h (kg m^{-3})	$\rho_b(host)$ (kg m^{-3})	ρ^*	ρ_b^*	η_h (Pa s)	U_{mf} (m s^{-1})	U_{inj} (m s^{-1})
A1	2500	3012	0	-0.2048	1	$2.956\ 10^{-4}$	$6.268\ 10^{-3}$
A2	2500	3012	0	-0.2048	5	$5.913\ 10^{-5}$	$1.254\ 10^{-3}$
A3	2500	3012	0	-0.2048	10	$2.957\ 10^{-5}$	$6.268\ 10^{-4}$
A4	2500	3012	0	-0.2048	50	$5.913\ 10^{-6}$	$1.254\ 10^{-4}$
A5	2500	3012	0	-0.2048	100	$2.957\ 10^{-6}$	$6.268\ 10^{-5}$
A6	2450	2994	0.02	-0.1976	1	$3.141\ 10^{-4}$	$6.660\ 10^{-3}$
A7	2450	2994	0.02	-0.1976	5	$6.283\ 10^{-5}$	$1.332\ 10^{-3}$
A8	2450	2994	0.02	-0.1976	10	$3.141\ 10^{-5}$	$6.660\ 10^{-4}$
A9	2450	2994	0.02	-0.1976	50	$6.283\ 10^{-6}$	$1.332\ 10^{-4}$
A10	2450	2994	0.02	-0.1976	100	$3.141\ 10^{-6}$	$6.660\ 10^{-5}$
A11	2550	3030	-0.02	-0.212	1	$2.772\ 10^{-4}$	$5.876\ 10^{-3}$
A12	2550	3030	-0.02	-0.212	5	$5.544\ 10^{-5}$	$1.175\ 10^{-3}$
A13	2550	3030	-0.02	-0.212	10	$2.772\ 10^{-5}$	$5.876\ 10^{-4}$
A14	2550	3030	-0.02	-0.212	50	$5.544\ 10^{-6}$	$1.175\ 10^{-4}$
A15	2550	3030	-0.02	-0.212	100	$2.772\ 10^{-6}$	$5.876\ 10^{-5}$
A16	2200	2904	0.12	-0.1616	1	$4.065\ 10^{-4}$	$8.618\ 10^{-3}$
A17	2200	2904	0.12	-0.1616	5	$8.130\ 10^{-5}$	$1.724\ 10^{-3}$
A18	2200	2904	0.12	-0.1616	10	$4.065\ 10^{-5}$	$8.618\ 10^{-4}$
A19	2200	2904	0.12	-0.1616	50	$8.130\ 10^{-6}$	$1.724\ 10^{-4}$
A20	2200	2904	0.12	-0.1616	100	$4.065\ 10^{-6}$	$8.618\ 10^{-5}$
A21	2150	2886	0.14	-0.1544	1	$4.250\ 10^{-4}$	$9.010\ 10^{-3}$
A22	2150	2886	0.14	-0.1544	5	$8.500\ 10^{-4}$	$1.802\ 10^{-3}$
A23	2150	2886	0.14	-0.1544	10	$4.250\ 10^{-5}$	$9.010\ 10^{-4}$
A24	2150	2886	0.14	-0.1544	50	$8.500\ 10^{-6}$	$1.802\ 10^{-4}$
A25	2150	2886	0.14	-0.1544	100	$4.250\ 10^{-6}$	$9.010\ 10^{-5}$
B1	2150	2886	0.14	-0.1544	100	$4.250\ 10^{-6}$	$4.250\ 10^{-3}$

Run nb.	ρ_h **(kg m^{-3})**	$\rho_b(host)$ **(kg m^{-3})**	ρ^*	ρ_b^*	η_h **(Pa s)**	U_{mf} **(m s^{-1})**	U_{inj} **(m s^{-1})**
B2	2150	2886	0.14	-0.1544	100	$4.250\ 10^{-6}$	$4.250\ 10^{-2}$
B3	2150	2886	0.14	-0.1544	100	$4.250\ 10^{-6}$	$4.250\ 10^{-1}$
B4	2150	2886	0.14	-0.1544	100	$4.250\ 10^{-6}$	$4.250\ 10^{0}$

Table 3: List of the simulation performed for this chapter and corresponding variables.

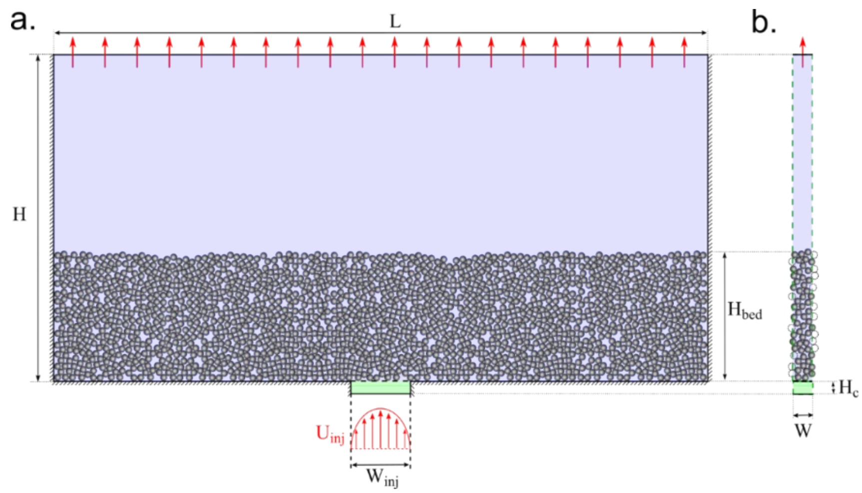

Figure 1: Simulations initial condition. [A] The drawing represents the computational domain viewed from the front. The medium is composed by rectangular box, which is fed by a conduit at its based. Particles are settled to generate a particle bed having a thickness H_{bed}. The background colors indicates which fluid is present initially in the computational domain. The blue color corresponds to the host melt and the green color to the intruded melt. The red arrows below the conduit represent the velocity profile of the injected fluid (Poiseuille flow). The arrows atop the domain indicate that the boundary condition is a fixed pressure outflow. The hatched walls indicate non-slip boundary conditions. [B] Side view of the computational domain. The green dashed lines indicate that cyclical boundary conditions are used for these walls. The dotted circles indicate particles overlapping with one of the two cyclical boundary conditions and that are also considered to be present on the opposite side.

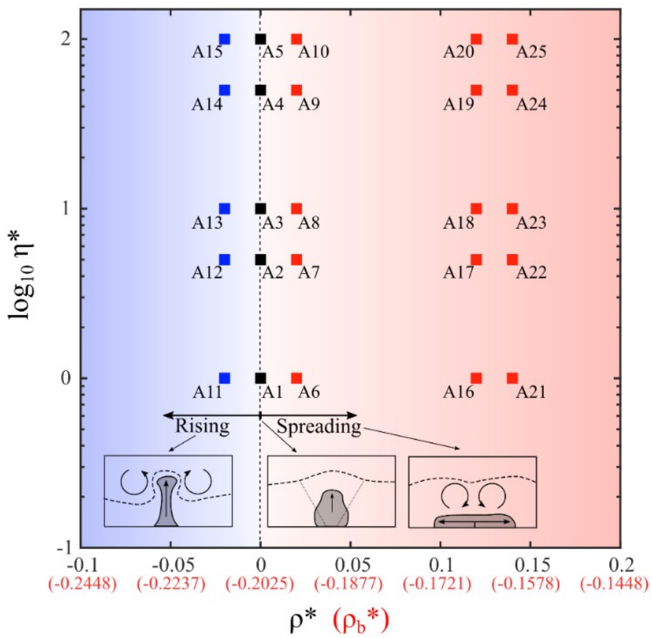

Figure 2: Regime diagram of intrusion behavior for U^*=21.2. The diagram represents the positions of the simulations A1–25 as functions of the reduced buoyancy (abscissa) and viscosity ratios (ordinate). Each square represents a simulation. Square colors depend on the observed regime (blue=rising; black=fluidization; red=lateral spreading). Similarly, the background color interpolates the observed regimes (blue= rising; red=lateral spreading) and the vertical dashed line interpolates where the fluidization is expected to prevail.

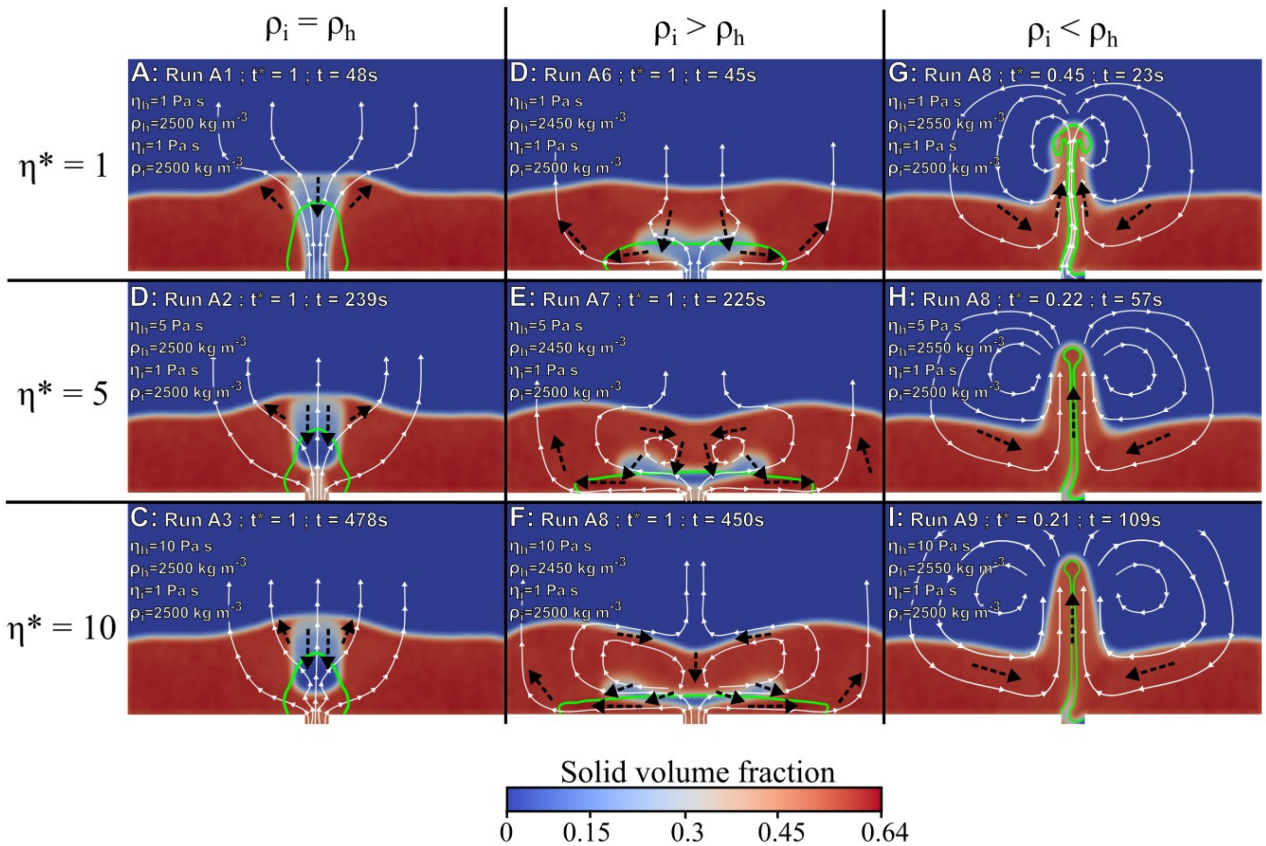

Figure 3: Comparison of the effects of buoyancy and viscosity contrasts. Each section represents the advancement of the simulation at t^{*}=1 (or when the rising instability is above the particle bed). The injected melt contours are indicated with green curves. The dashed black arrows indicate the presence and direction of granular flows. The thin white curves indicate the fluid streamlines with small arrowheads indicating flow direction.

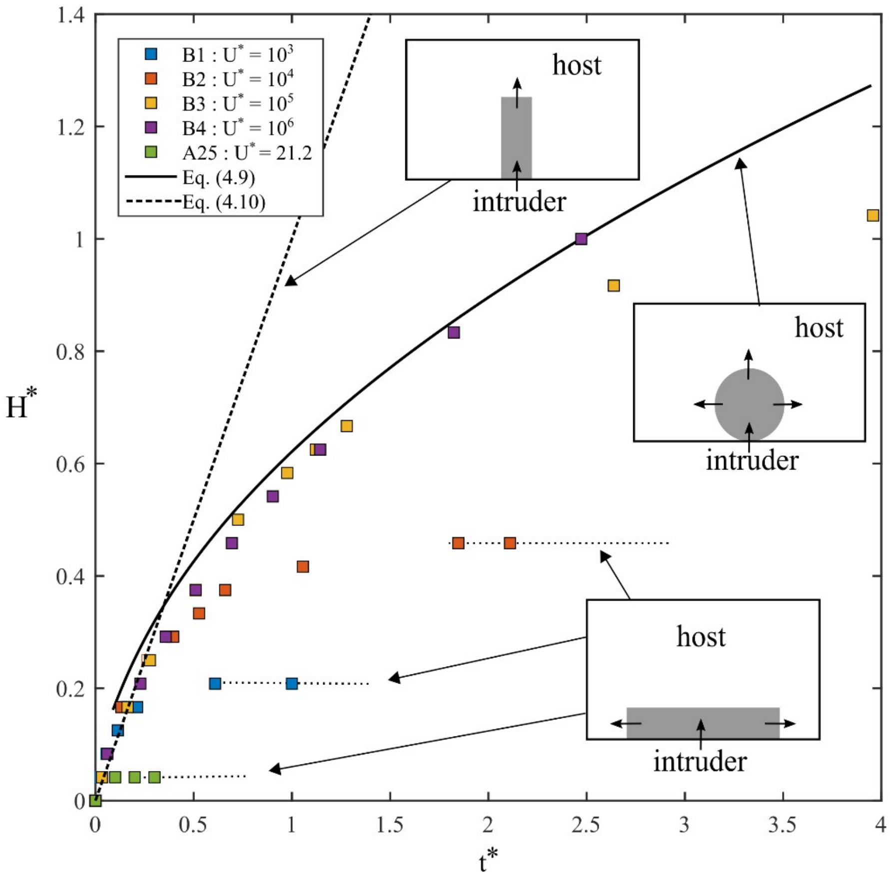

Figure 4: Evolution of the height, H^*, of the intruded volume as a function of the dimensionless time t^*. Each square represents the height of the top of the intruded volume measured in the simulations. Square colors indicate injection rate. Dashed lines indicate the theoretical intruder front height evolution in the case of vertical propagation (supplementary information 3) The black curve is the theoretical front height for a radial growth, and the horizontal dotted lines indicate the front height evolution during lateral spreading. The three insets illustrate intrusion behaviors.

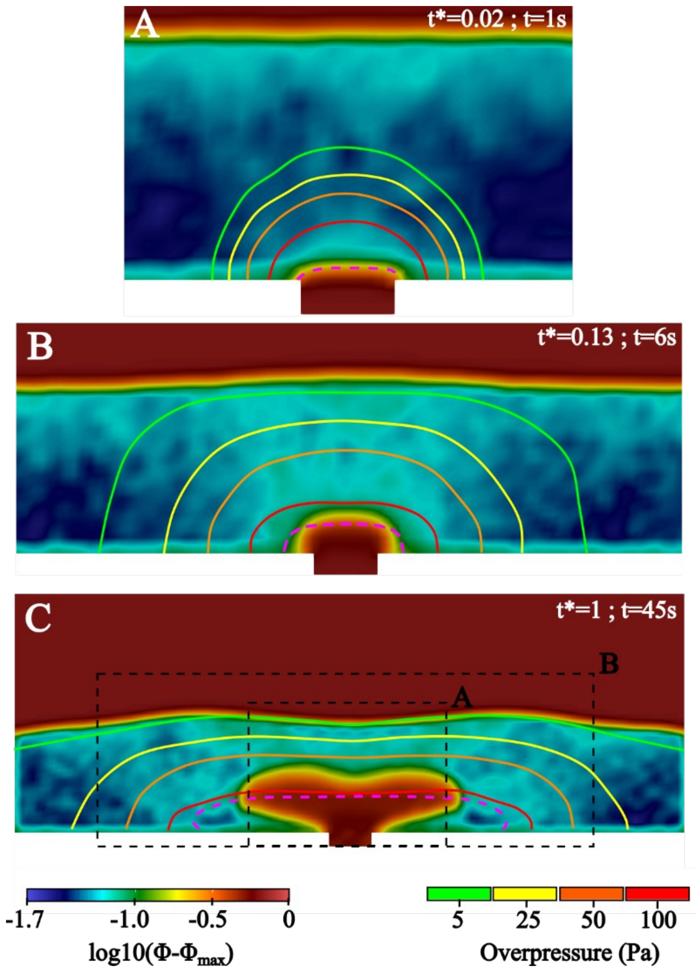

Figure 5: Evolution of the pore pressure and crystal volume fraction. On each inset, the color depend on the difference between the local crystal volume fraction, Φ, and the maximum one, Φ_{max} (Φ_{max}=0.64), in a logarithmic scale. The overpressure respect to the initial hydrostatic pressure field is indicated with contour that corresponds to the isosurfaces where the overpressure are equal to 5, 25, 50, and 100 Pa. The pink dashed curves represent the boundary between the injected and resident melt. Inset [A] and [B] are captured after 1s and 6s. Both only displayed the portion of the mush layer that present overpressure and dilation. Inset [C] is acquired after 45s and cover a slice of the entire computational domain. The two dashed rectangle indicate the extend of insets [A] and [B].

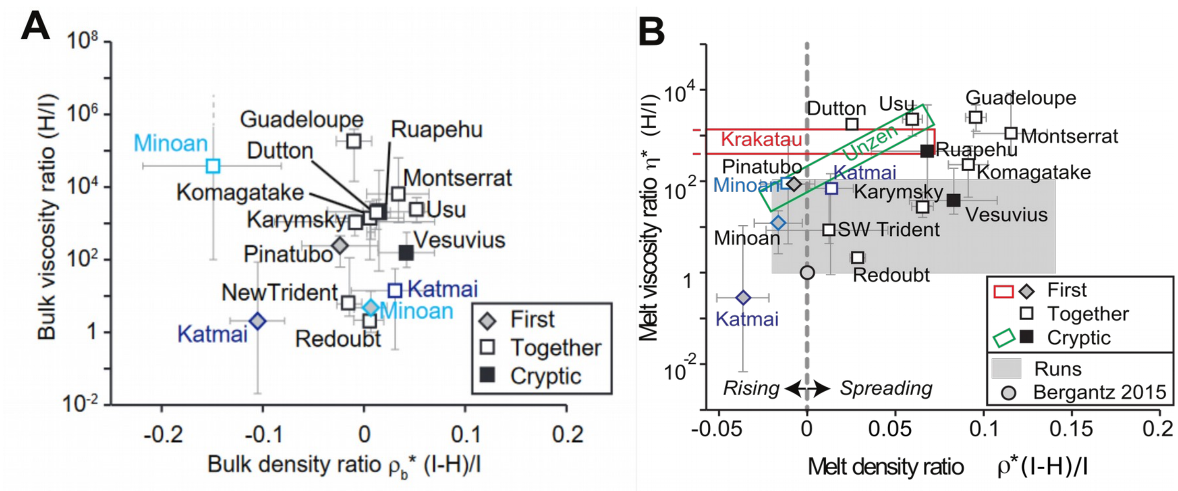

Figure 6: [A] Ratios of bulk properties for the host and intruder magmas involved in 15 eruptions. The bulk viscosity ratio is that of the host over that of the intruder and the bulk density ratio is that of the difference between the intruder and the host over that of the intruder. Eruptions are sorted according to whether the intruder magma was erupted first ("First"), at the same time as (or mixed with) the host ("Together"), or fully mixed with the host ("Cryptic"). [B] Ratios of melt properties for the host and intruder magmas involved in 15 eruptions. The melt viscosity ratio is that of the host over that of the intruder and the melt density ratio is that of the difference between the intruder and the host over that of the intruder. Eruptions are sorted according to whether the intruder magma was erupted first ("First"), at the same time as (or mixed with) the host ("Together"), or fully mixed with the host ("Cryptic"). The gray area covers the runs done in this study and the cross marks the parameters used in the numerical study of Bergantz et al. (2015). See text for details regarding the special cases of Unzen and Krakatau.

Supplementary Information 1:

This Supplementary Information includes two tables summarizing the equation system solved in our numerical simulations (Tables S1–S2).

Table S1: List of the equations implemented in the CFD-DEM model

Equation names	Equations	Ref.
Mass conservation	$\frac{\partial \varepsilon_f}{\partial t} + \nabla \cdot (\varepsilon_f \vec{v}_f) = 0$	1
Momentum conservation	$\rho_f \left(\frac{\partial}{\partial t}(\varepsilon_f \vec{v}_f) + \nabla \cdot (\varepsilon_f \vec{v}_f \otimes \vec{v}_f) \right) = \nabla \cdot (\acute{\sigma}_f) + \varepsilon_f \rho_f \vec{g} + \vec{I}_f$	1
Stress tensor	$\acute{\sigma}_f = P_f \delta_{ij} + \frac{2}{3} \eta_f tr(\acute{\epsilon}_f) \delta_{ij} + 2 \eta_f \acute{\epsilon}_f$	1
Euler velocity integration	$\vec{v}_p^{(k)}(t+\Delta t) = \vec{v}_p^{(k)}(t) + \Delta t \frac{\overrightarrow{F_{GPD}}^{(k)}(t) + \sum_{l=1}^{N_l^{(k)}} \left(\overrightarrow{F_C^{N(k,l)}}(t) + \overrightarrow{F_C^{T(k,l)}}(t) \right)}{m^{(k)}}$	Eq. (4.4)
Euler displacement integration	$\vec{X}_p^{(k)}(t+\Delta t) = \vec{X}_p^{(k)}(t) + \Delta t \vec{v}_p^{(k)}(t+\Delta t)$	2
Euler rotation integration	$\vec{\omega}_p^{(k)}(t+\Delta t) = \vec{\omega}_p^{(k)}(t) + \Delta t \frac{\sum_{l=1}^{N_l^{(k)}} \left(\vec{T}_C^{(k,l)} + \vec{T}_L^{(k,l)}(t) \right)}{I^{(k)}}$	2
Normal contact force	$\vec{F}_c^{N(i,j)}(t) = \left(-k_n^{(i,j)}(t) \delta_n^{(i,j)}(t) + \eta_n^{(i,j)}(t) \Delta \vec{V}_p^{N(i,j)}(t) \right) \vec{n}_{ij}$	2 5
Tangential contact force	$\vec{F}_c^{T(i,j)}(t) = -k_t^{(i,j)}(t) \delta_t^{(i,j)}(t) + \eta_t^{(i,j)}(t) \overrightarrow{\Delta V}_p^{T(i,j)}(t)$	2 5
Collisional torque	$\vec{T}_c^{(i,j)}(t) = \frac{d_p^{(i)} - \delta_n^{(i,j)}(t)}{2} \vec{F}_c^{T(i,j)}(t) ; \vec{T}_c^{(j,i)}(t) = \frac{d_p^{(j)} - \delta_n^{(i,j)}(t)}{2} \vec{F}_c^{T(i,j)}(t)$	2
normal spring (Hertzian model)	$k_n^{(i,j)}(t) = \frac{4}{3} \frac{E^{(i)} E^{(j)} \sqrt{R_{eff}^{(i,j)}}}{E^{(j)}(1-\sigma^{(i)2}) + E^{(i)}(1-\sigma^{(j)2})} \delta_n^{(i,j)\frac{1}{2}}(t)$	2
tangential spring (Hertzian model)	$k_t^{(i,j)}(t) = \frac{16}{3} \frac{G^{(i)} G^{(j)} \sqrt{R_{eff}^{(i,j)}}}{G^{(j)}(2-\sigma^{(i)}) + G^{(i)}(2-\sigma^{(j)})} \delta_t^{(i,j)\frac{1}{2}}(t)$	2
Elastic modulus	$G = \frac{E}{2(1+\sigma)}$	2

Equation names	Equations	Ref.
Normal damping coefficient	$\eta_n^{(i,j)}(t)=\frac{2\sqrt{m_{eff}^{(i,j)}k_n^{(i,j)}(t)}\left\|\ln e_n\right\|}{\sqrt{\pi^2+\ln^2 e_n}}\delta_n^{(i,j)}(t)^{\frac{1}{4}}$	2 5
Tangential damping coefficient	$\eta_t^{(i,j)}=\frac{2\sqrt{m_{eff}^{(i,j)}k_t^{(i,j)}(t)}\left\|\ln e_t\right\|}{\sqrt{\pi^2+\ln^2 e_t}}\delta_t^{(i,j)}(t)^{\frac{1}{4}}$	2 5
effective radius	$R_{eff}^{(i,j)}=\frac{2\left(d\|p^{(i)}+d_p^{(j)}\right)}{d_p^{(i)}d_p^{(j)}}$	2
Effective mass	$m_{eff}^{(i,j)}=\frac{m^{(i)}+m^{(j)}}{m^{(i)}m^{(j)}}$	2
Solids/Fluid momentum exchange on REV	$\vec{I}_f(t)=\frac{1}{v_{REV}}\sum_{k=1}^{N_k}\vec{F}_D^{(k)}(t)\,K_{REV}\left(X_p^{(k)}\right)$	2
Drag forces (for the fluid)	$\vec{F}_D^{(k)}(t)=-\nabla P_f(t)\left(\frac{\pi}{6}d_p^{(k)3}\right)+\frac{\beta_{fs}^{(k)}(t)}{\left(1-\varepsilon_f(t)\right)}\left(\frac{\pi}{6}d_p^{(k)3}\right)\left(\vec{v}_f(t)-\vec{v}_p^{(k)}(t)\right)$	2
Local fluid/solid momentum transfer	$\beta_{fs}^{(k)}(t)=\begin{cases}\frac{3}{4}C_D^{(k)}(t)\frac{\rho_f\varepsilon_f(t)\left(1-\varepsilon_f\right)\left\|\vec{v}_f-\vec{v}_s^{(k)}\right\|}{d_p^{(k)}}\varepsilon_f^{-2.65}\ \varepsilon_f\geq 0.8\\ \frac{150\left(1-\varepsilon_f(t)\right)^2\eta_f}{\varepsilon_f(t)d_p^{(k)2}}+\frac{1.75\rho_f\left(1-\varepsilon_f(t)\right)\left\|\vec{v}_f(t)-\vec{v}_s^{(k)}(t)\right\|}{d_p^{(k)}}\varepsilon_f\end{cases}$	3 4
Drag coefficient	$C_D^{(k)}(t)=\begin{cases}\frac{24}{Re^{(k)}(t)\left(1+0.15\,Re^{(k)}(t)^{0.687}\right)}\ Re^{(k)}(t)<1000\\ 0.44\ Re^{(k)}(t)\geq 1000\end{cases}$	3 4
Particle Gravity-Drag-Pressure force	$\overrightarrow{F_{GPD}}(t)=\frac{m_p}{\Delta t}\left(\vec{v}_f+\tau_v\left(\vec{g}-\frac{\nabla P}{\rho_p}\right)-\vec{v}_p(t)\right)\left(1-e^{\frac{-\Delta t}{\tau_v}}\right)$	Eq. (4.5)
Reynolds number	$Re^{(k)}(t)=\frac{d_m^{(k)}\left\|\vec{v}_f(t)-\vec{v}_s^{(k)}(t)\right\|\rho_f}{\eta_f}$	3

[1] Syamlal et al., (1993)

[2] Garg et al., (2010)

[3] Benyahia et al., (2012)

[4] Gidaspow, (1986)

Table S2 : Symbols used in Table S1

Symbol	Definition
$C_D^{(k)}$	Drag coefficient of the kth particle
$d_p^{(i)}$	ith particle diameter
e_n	Particle normal restitution coefficient
e_t	Particle tangential restitution coefficient
$E^{(i)}$	ith particle Young modulus
$\overrightarrow{F_C^{N(k,l)}}$	Normal contact force between kth particle and its lth neighbor
$\overrightarrow{F_C^{T(k,l)}}$	Tangential contact forces between kth particle and its lth neighbor
$\overrightarrow{F_D}^{(k)}$	Drag force on kth particle
$\vec{g}$	Gravitational vector (m s^{-2})
$G^{(k)}$	kth particle shear moduli
$h^{(i,j)}$	Distance between ith and jth particles edges
$\vec{I}_f$	Fluid-solid momentum exchange
$I^{(k)}$	kth particle moment of inertia
K_{REM}	Generic kernel to determine the influence of a particle located at $\overrightarrow{X_p}^{(k)}$ on the REV
$k_n^{(i,j)}$	Normal spring coefficient between ith and jth particles contact
$k_t^{(i,j)}$	Tangential spring coefficient between ith and jth particles contact
l	Neighbors index
$m^{(k)}$	kth particle mass
$m_{eff}^{(i,j)}$	ith and jth particles effective radius
$N_l^{(k)}$	Number of neighbors of the kth particle
N_k	Number of particles
$\vec{n}_{ij}$	Normal vector between ith and jth particles
P_f	Fluid pressure (Pa)

REV	Representative elementary volume
$Re^{(k)}$	i^{th} particle Reynolds number
$R_{eff}^{(i,j)}$	i^{th} and j^{th} particles effective radius
$R_{\square}^{(i,j)}$	Contact area radius between i^{th} and j^{th} particles
$\overrightarrow{T}_C^{(k,l)}$	Contact torque between k^{th} particle and its l^{th} neighbor
$\overrightarrow{T}_L^{(k,l)}$	Lubrication torque between k^{th} particle and its l^{th} neighbor
$\vec{v}_f$	Fluid velocity vector (m s^{-1})
$\overrightarrow{v}_p^{(k)}$	k^{th} particle velocity vector (m s^{-1})
$\overrightarrow{X}_p^{(k)}$	k^{th} particle position (m)
$\beta_{fs}^{(k)}$	k^{th} particle – fluid momentum transfer coefficient
$\Delta V_p^{N(i,j}$	Normal relative velocity between i^{th} and j^{th} particles
$\Delta V_p^{T(i,j)}$	Tangential relative velocity between i^{th} and j^{th} particles
δ_{ij}	Kronecker tensor
$\delta_n^{(i,j)}$	Normal overlap between i^{th} and j^{th} particles
$\delta_t^{(i,j)}$	Tangential displacement during the contact between i^{th} and j^{th} particles contact
ε	Roughness distance below which lubrication is ineffective (m)
ε_f	Fluid volume fraction
$\acute{\epsilon}_f$	Fluid strain rate tensor
η_f	Fluid viscosity (Pa s)
$\eta_n^{(i,j)}$	Normal damping coefficient between i^{th} and j^{th} particles
$\eta_t^{(i,j)}$	Tangential damping coefficient between i^{th} and j^{th} particles
v	Domain volume (m^{-3})
ρ_f	Fluid density (kg m^{-3})
$\sigma^{(i)}$	i^{th} particle Poisson coefficient
$\acute{\sigma}_f$	Fluid stress tensor
$\overrightarrow{\omega}_p^{(k)}$	k^{th} particle rotation vector (rad s^{-1})

∇	Nabla operator
$\otimes$	Outer product

Supplementary Information 2:

This supplementary information presents an updated derivation of the minimum fluidization velocity compared to those used in the literature.

The onset of fluidization of a crystal bed occurs when the upward drag force exerted by the injected fluid exceed its net weight. Shi et al. (1984) proposed a formula to predict the minimum fluidization velocity of a random packed bed due to a localized injection of fluid. These authors made the assumption that the fluid velocity is only vertical and uniformly distributed on horizontal cross-sectional area (Fig. S1). The total upward drag force is computed with the Ergun's formula (Ergun, 1952) for a bed fluidized uniformly. Later, Cui et al. (2014) adapted this formula by considering the fluid velocity uniform along a semi-circular cross sectional area. Here, we modify the approach of Cui et al. (2014) to predict the minimum fluidization velocity in the experimental apparatus geometry because the original derivation incorrectly assumed the distance between the injection point and center of the inlet, r_0 , and the boundaries of the integral in their Eq. (13).

The total upward drag force applied by the inlet on the particle bed is computed as:

$$F_D = \int_{r_0}^{H+r_0} \left(A U_r + B U_r^{\,2} \right) S(r)\, dr, \qquad \text{(S1)}$$

where r_0 correspond of the vertical coordinates of the bottom and $H+r_0$ is the position of the top of the particle bed. The variable r corresponds to the radial distance from a hypothetic injection point (Fig. S1). A and B are given by Ergun (1952):

$$A = 150 \frac{\phi^2}{(1-\phi)^3} \frac{\eta_f}{d_p^{\,2}}, \qquad \text{(S2)}$$

$$B = 1.75 \frac{\phi}{\left(1-\phi\right)^3} \frac{\rho_f}{d_p}. \tag{S3}$$

$S\left(r\right)$ represents the area of the curved surface on which the fluid velocity is uniform, and it is computed as a function of r as:

$$S\left(r\right) = 2\alpha\left(r + r_0\right) W_l. \tag{S4}$$

U_r is the fluid velocity at a radial distance r. U_r may be computed by considering that the injected flux is conserved through the particle bed height, which yields:

$$Q_{inj} = U_r S\left(r\right), \tag{S5}$$

and, with (S4):

$$U_r = \frac{Q_{inj}}{2\alpha\left(r + r_0\right) W_l} \tag{S6}$$

Substituting Eqs. (S6) and (S4) into Eq. (S1) yields:

$$F = A Q_{inj} H_0 + \frac{B {Q_{inj}}^2}{2\alpha W_l} \ln\left(\frac{H_0 + 2r_0}{2r_0}\right) \tag{S7}$$

In this geometry, the net weight of the bed, W, is given by:

$$W = \left[\left(r_0 + H_0\right)^2 \tan\alpha - \frac{W_{inj} r_0}{2}\right] W_l \left(\rho_p - \rho_f\right) g \phi. \tag{S8}$$

Introducing $r_0 = W_{inj} / \left(2\tan\alpha\right)$, the onset of fluidization occurred when $F = W$, which yields:

$$A Q_{inj} H_0 + \frac{B {Q_{inj}}^2}{2\alpha W_l} \ln\left(\frac{2\tan\alpha}{W_{inj}} + 1\right) - \left[H_0\left(W_{inj} + H_0 \tan\alpha\right)\right] W_l \left(\rho_p - \rho_f\right) g \phi = 0 \tag{S9}$$

Figure S2 displays comparison of the minimum fluidization velocities computed with formulas from Ergun (1952), Shi et al. (1984), Cui et al., (2014), and Eq. (S9), function of the particle bed height. It shows that Eq (S9) is closer to the result predicted with the formulas from Ergun (1952) and Shi et al. (1984). The incorrect formula derived by Cui et al., (2014) results in the significant overestimations of the minimum fluidization velocity.

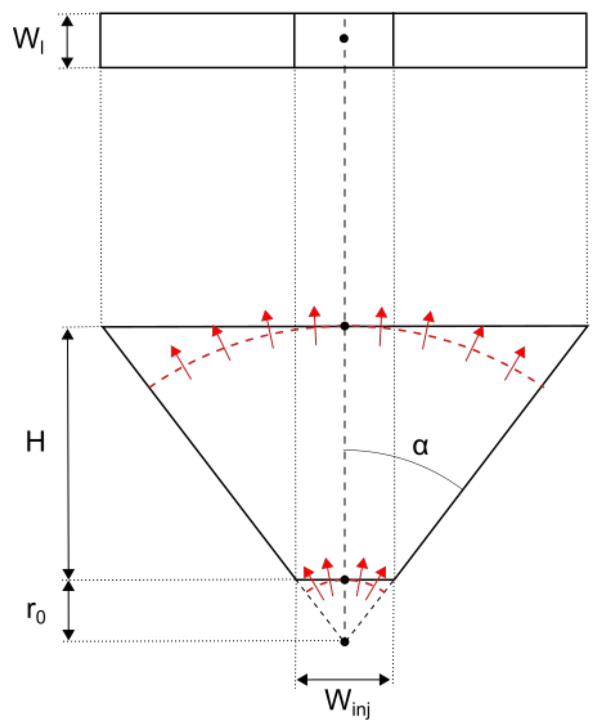

Figure S1: Conceptual framework to derive the minimum fluidization velocity. The top draw is a view from the top. The bottom draw is a front view. On both draws, the thick black lines represent the boundaries of the volume of the particle bed, which is fluidized. The red dashed curves indicate the cross sectional areas where the magnitude of the fluid velocity is uniform. The arrows represent the direction of the fluid flow. The black dots represent the positions of the theoretical injections point and intersections between the cross sectional areas where the fluid velocity is uniform and the vertical boundary of the fluidized particle bed.

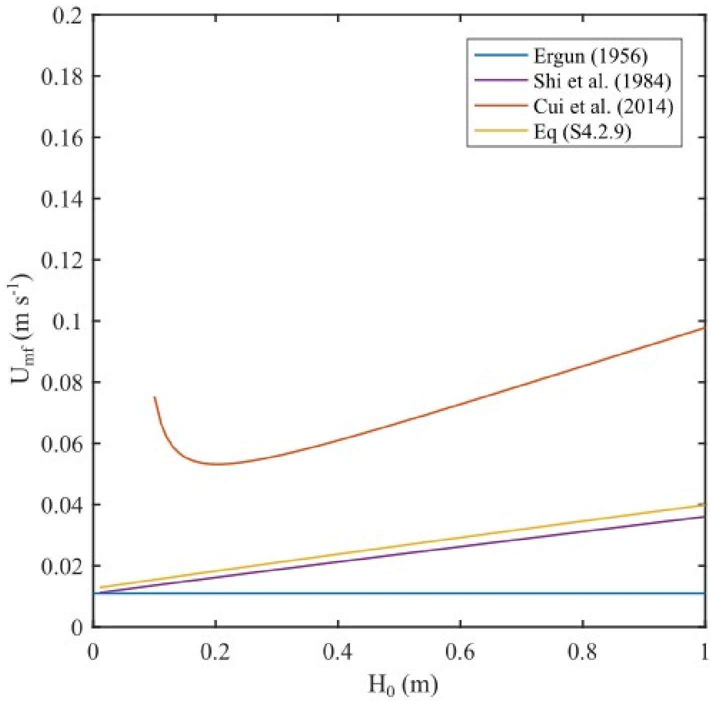

Figure S2: Comparison of the minimum fluidization velocities function of the initial particle bed height. The curves represent the minimum fluidization velocities derived by authors and the one given here.

Supplementary Information 3:

This supplementary information presents the derivation of the maximum height of the intrusion as a function of the time for end member scenarios.

We consider two end-members for the growth of the intrusion volume (vertical or radial). The first end member considers the vertical ascent (dyking) of the intruded melt above the inlet over a width, W_{inj}. In this case, the ratio, H^*, between H_{max} and the initial particle bed thickness, H_{bed} ($H^*=H_{max}/H_{bed}$), reads:

$$H^*=t^*. \tag{S10}$$

In the case of radial growth, we consider as spherical intrusion having a unknown radius, R, and fed by an inlet of width W_{inj} (Fig. S3). The inlet truncates the sphere at a vertical distance, h, which depends on both R and W_{inj}. The objective is to compute the distance from the inlet to the top of the sphere, H, knowing the area A and injection width W_{inj}. The total area, A_{tot}, of the sphere is the sum of the area A, where the intruded fluid is present and the truncated area B as:

$$A_{tot}=A+B. \tag{S11}$$

The area A depends on injection velocity and time. The area A_{tot} may be expressed using the sphere radius R. Replacing A and A_{tot} in equation (S11) and rearranging yields:

$$\pi R^2=W_{inj}H_{bed}t^*+A_B. \tag{S12}$$

The area B may be approximated with a good accuracy as (Harris and Stöcker, 1998, pp 92-93):

$$A_B\approx\frac{2}{3}W_{inj}h+\frac{h^3}{2W_{inj}}. \tag{S13}$$

Inserting Eq. (S13) in Eq. (S12) gives:

$$0=W_{inj}H_{bed}t^*+\frac{2}{3}W_{inj}h+\frac{h^3}{2W_{inj}}-\pi R^2. \tag{S14}$$

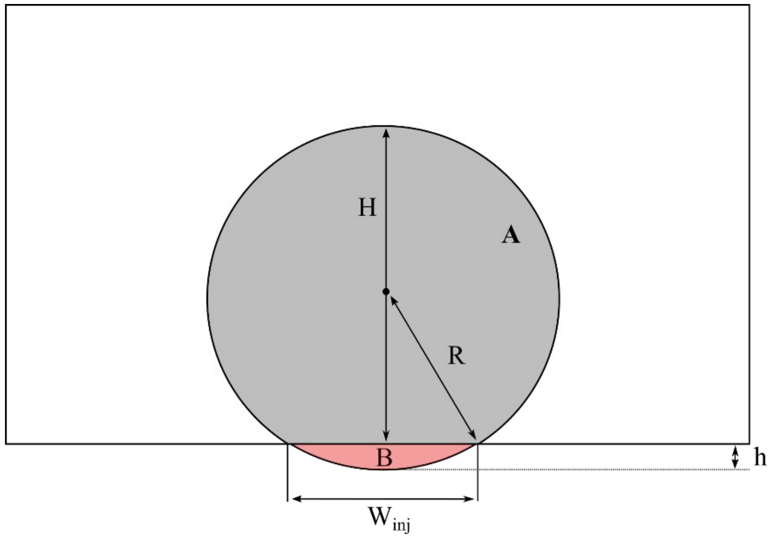

Equation (S14) contains two unknowns, R and h, which can be related to each other tanks to geometry:

$$0 = \frac{{W_{inj}}^2}{4} + (R-h)^2 - R^2. \qquad \text{(S15)}$$

Using that $H = 2R - h$, H_{max} may be computed as a function of t^* by solving Equations (S14–S15).

Figure S3: Schematics of the geometrical setup. The drawing represents a section perpendicular to the intrusion. The area covered by the injected melt is in gray and the area

Supplementary information 4:

This supplementary figures displays the magnitude of the vorticity.

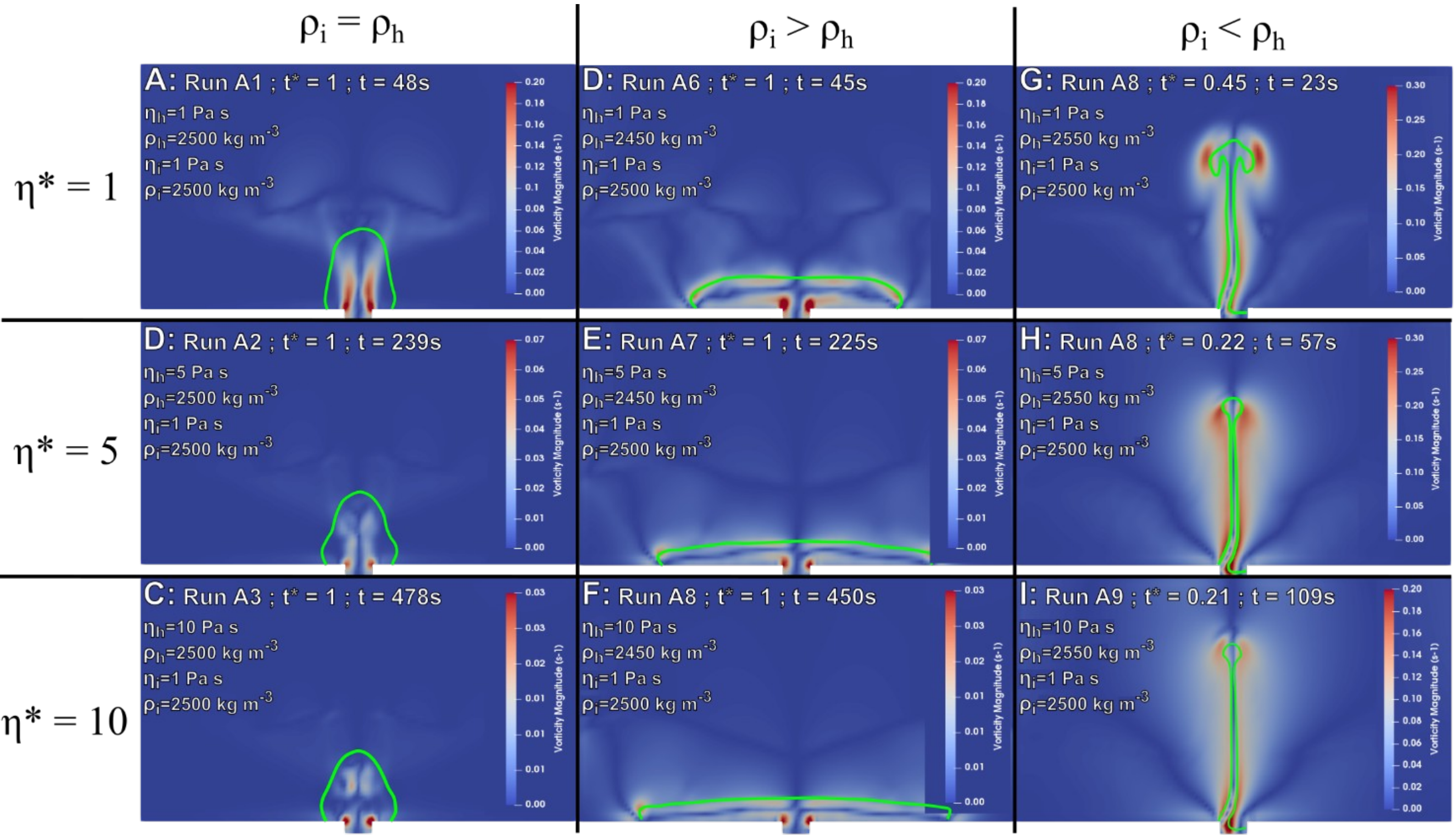

Figure S4: Magnitude of the vorticity. Simulations correspond to the ones represented in Fig. 3 for the same time steps. The green curves indicate the injected melt contour.

Supplementary information 5:

This supplementary section present the physical properties of the end members materials involved in the 15 eruption considered in this study. In cases where mixing was so preeminent that only mixed products were erupted (e.g., Unzen), pre-mixing host characteristics, including crystal content, were determined using indirect evidences such as crystal rims in disequilibrium with the surrounding melt. Viscosities and densities of intruder magmas were sometimes directly characterized because they were erupted (e.g., Pinatubo; Pallister et al., 1996) or approximated using petrological inferences (e.g., Usu, where the melt SiO_2 content was estimated by Tomiya and Takahashi, 1995, from mixing lines and end-members). The software Conflow (Mastin, 2002) was used to calculate densities and viscosities when necessary.

All host magmas are mushes except one simple case and three complex cases. The Usu reservoir contained a nearly aphyric (2–5 vol.% crystals) rhyolite prior to the 1663 eruption (Tomiya and Takahashi, 1995). We left this straightforward case in our analysis for completeness; removing it would not affect our results. We treated the next three complex cases separately in our analysis. Krakatau is a compositionally zoned reservoir with a gradient in crystal content ranging from 4–15 vol.% in the felsic (dacitic to rhyodacitic) parts of the reservoir to aphiric in the more mafic (andesite) parts of the reservoir (Mandeville et al., 1996). The second case is the Bronze Age eruption of Santorini volcano known as the Minoan eruption. In one scenario, the reservoir that hosted the Minoan eruption products had 10–20 vol% crystals (Cadoux et al., 2014). In others, more complex scenarios have been proposed (Druitt, 2014; Flaherty et al., 2018; Martin et al., 2010). In one, the main rhyodacite would have instead acted as the intruder into an adjacent mushy, mafic reservoir (Druitt, 2014). We reported these two possibilities. The 1912 eruption at Katmai–Novarupta is also a case where the roles of the intruder and host might be reversed (e.g. Coombs and Gardner, 2001; Eichelberger and Izbekov, 2000; Hammer et al., 2002; Singer et al., 2016). We reported the scenario in which the most crystal-rich components (andesite and dacite) are the hosts and the nearly aphyric rhyolite is the intruder (Eichelberger and Izbekov, 2000), as well as the scenario in which the host is composed of a zoned chamber and the intruder is a basaltic andesite (Singer et al., 2016).

There is a last complex case that is analyzed individually although its reservoir unambiguously contained a mush. Two mutually exclusive intrusion scenarios have indeed been proposed to explain the 1991–1995 eruption of Unzen volcano. In both scenarios, the host magma was a phenocryst-rich, low-temperature rhyolite mush and the intruder was a nearly aphyric, high-temperature magma (Holtz et al., 2004; Nakamura, 1995). The composition of the intruder, which left only cryptic indications of its presence such as reverse zoning of the outer rims of hornblende, plagioclase and magnetite (Nakamura, 1995), could have been either andesitic (Holtz et al., 2004), or basaltic (Browne et al., 2006).

Table S3: Host properties from natural cases (volcano names are followed by the starting year of the eruption). Minerals abbreviations are plagioclase (Plag), clinopyroxene (CPx), orthopyroxene (OPx), pyroxene (Px), and hornblende (Hb). Only the main mineral phases were taken into account and numbers in parenthesis are mineral volume proportions. Bulk densities were calculated with a plagioclase density of 2570 kg/m^3 and a density of 3200 kg/m^3 for all other minerals. Bulk viscosities were calculated as $\eta_l\left(1-\varphi/0.6\right)^{-2.5\cdot 0.6}$, where η_l is melt viscosity and φ is crystal volume fraction, except for the Minoan scenario 2 where the largest bul viscosity was capped at 10^{10} Pa s because the higher bound of φ is >0.6. Abbreviations sat. and usat. mean saturated and undersaturated, respectively. Not used (n.u.) implies that melt densities and/or viscosities were directly given in the reference(s) corresponding to that case.

CASE	Name	Xtal (vol%)	Minerals	Melt SiO_2 (wt%)	Melt H_2O (wt%)	Melt density (kg/m^3)	Melt viscosity (Pa s)	T (°C)	P (MPa)	Ref
Unzen 1991	Dacite	34-35	Plag (0.8) Cpx (0.2)	75	8	2229-2239	1.3×10^{4}-1.4×10^{4}	775	300	1
Vesuvius -79	White Pumice	31.6-40	Plag	53-57	sat.	2218-2300	2.4×10^{3}-3.0×10^{3}	875-900	150 [b]	2
Guadeloupe 1530	Andesite	48.3-57.5	Plag (0.8) Px (0.2)	73-75	5.5-6	2189-2203	1.2×10^{4}-2.5×10^{4}	825-875	135-200	3
Karymsky 1996	Andesite	25-32	Plag (0.8) Px (0.2)	63	sat.	2395-2378 [a]	8.9×10^{3}-13×10^{3} [a]	1023-1057	200 [b]	4
Ruapehu 1995	Andesite	24.5-42	Plag (0.66) Px (0.33)	62-70	1-1.5	2380-2438	2.9×10^{4}-4.7×10^{4}	920-1030	40	5
Katmai 1912 – scenario 1	Andesite	30-45	Plag (0.8) Px (0.2)	67.6-74	usat-sat.	2274-2284	1.2×10^{4}-1.3×10^{4}	920-970	75-120	6
	Dacite	30-45	Plag (0.8) Px (0.2)	79.1	usat-sat.	2189-2220	2.0×10^{5}-8.1×10^{5}	850-910	60-25	
Katmai 1912 – scenario 2	Andesite	30	Plag (0.8) Px (0.2)	67.6	usat.	2274	1.2×10^{4}	920	75	7
	Rhyolite	2	Plag	77	4	2225	1.7×10^{6}	790	40	
Komagatake 1640	White Pumice	25-43.1	n.u.	74.7-76.1	3-4	2280-2300	4.4×10^{4}-2.9×10^{5} [a]	970-980	n.u.	8
Montserrat 1995	Andesite	35-45	Plag	75-80	4.8	2171-2160	3.7×10^{4}-8.4×10^{4}	835-880	105-155	9
Redoubt 1990	Dacite	24-32	Plag	78.5-81	4	2164-2174	3.4×10^{4}-3.8×10^{4}	840-950	100	10

Krakatau 1883	White Rhyodacite	7-15	Plag	70-74	4	2220-2400	3.1×10^4-3.4×10^4	880-890	100-150	11
	Gray Dacite	4-12	Plag	66.5-75	4	2190-2200	1.3×10^4-1.4×10^4	890-913	100-150	
Minoan – scenario 1	Rhyodacite	10-20	Plag	73.5-74	5-6	2222-2173	1.7×10^4-1.4×10^5	845-860	200-250	12
Minoan – scenario 2	Andesite	55-100	Plag (0.8) CPx (0.2)	71-77	sat. [b]	2213-2231	5.9×10^5-1.3×10^7	700-820	50	13
SW Trident 1953	Dacite	37-39	Plag (0.8) Px (0.2)	75	3.6	2190-2200	4.5×10^4-4.9×10^4	890	90	14
Dutton 1989	Dacite	35	Plag (0.8) OPx (0.2)	78	sat.	2481-2491	1.4×10^5-1.5×10^5	865	200 [b]	15
Pinatubo 1991	White Pumice	47	Plag (0.8) Hb (0.2)	76	6-6.5	2166	5.4×10^4	750-800	155-200	16
	Tan Pumice	15-26	Plag (0.8) Hb (0.2)	73	6-6.5	2194	5.6×10^4	750-800	155-200	
Usu 1663	Silicic magma	2.6-5.3	Plag (0.8) OPx (0.2)	74	n.u.	2210-2224	9.5×10^4-2.6×10^5	750-800	n.u.	17

[a] Calculated from bulk values given in the reference(s).

[b] Assumed value.

[c] References are: 1) Holtz et al. (2005), Vetere et al. (2008)(andesite intruder), Browne et al. (2006)(basalt intruder); 2) Cioni et al. (1995), Scaillet et al. (2008); 3) Pichavant et al. (2018); 4) Izbekov et al. (2002), Izbekov et al. (2004), Eichelberger and Izbekov (2000); 5) Nakagawa et al. (1999), Nakagawa et al. (2002), Kilgour et al. (2013); 6) Eichelberger and Izbekov (2000), Coombs and Gardner (2001); 7) Hammer et al. (2002), Singer et al. (2016); 8) Takahashi and Nakagawa (2013); 9) Barclay et al. (1998), Murphy et al. (2000), Couch et al. (2001), Humphreys et al. (2010), Plail et al. (2018); 10) Wolf and Eichelbeger (1997), Nye et al. (1994), Swanson et al. (1994); 11) Camus et al. (1987), Self (1992), Mandeville et al. (1996); 12) Cottrell et al. (1999), Druitt et al. (1999), Cadoux et al. (2014), Flaherty et al. (2018); 13) Druitt (2014); 14) Coombs et al. (2000), Coombs et al. (2002); 15) Miller et al. (1999); 16) Pallister et al. (1992), Pallister et al. (1996), Bernard et al. (1996); 17) Tomiya and Takahashi (2005).

Table S4: Intruder properties from natural cases. Minerals abbreviations are plagioclase (Plag), clinopyroxene (CPx),, pyroxene (Px), hornblende (Hb), olivine (Ol), and Augite (Aug). Abbreviations and references are the same as in Table S1.

CASE	Name	Xtal (vol%)	Minerals	Melt SiO_2 (wt%)	Melt H_2O (wt%)	Melt density (kg/m^3)	Melt viscosity (Pa s)	T (°C)	P (MPa)
Unzen 1991	Andesite	0-10	Plag [b]	62-64	4	2184-2194	3.2×10^2-3.2×10^2	1030-1130	300
	Basalt	0-5	Ol	50	sat. [b]	2351-2418	2.3-10	1030-1200 [b]	300 [b]
Vesuvius -79	K-rich basalt	0-20	Plag	50-52	usat.	2485-2441	13-16	1050-1140	150 [b]
Guadeloupe 1530	Basalt	0-12	Plag	50-53	5-6	2436-2420	5.4-9.3	975-1025	200 [b]
Karymsky 1996	Basalt	20	Plag	52	sat.	2545 [a]	22-54	1080-1115	200 [b]
Ruapehu 1995	High-T magma	0-10	Plag [b]	54.2-57.7	1-1.5	2530-2640	10-10^2	1100 [b] -1200 [b]	40
Katmai 1912 – scenario 1	Rhyolite	2	Plag	77	4	2225-2172	7.5×10^3-1.7×10^6	790-850	40-100
Katmai 1912 – scenario 2	Andesite	30-45	Plag (0.8) Px (0.2)	67.6-74	usat.-sat.	2274-2284	1.2×10^4-1.3×10^4	920-970	75-120
Komagatake 1640	Basalt	0		57	n.u.	2500 [b]-2540	5.0×10^3-1.0×10^3 [a]	1150	n.u.
Montserrat 1995	Mafic recharge	2-4.5	Plag	52-71	sat.	2400-2500	10-10^2	975-1196	105-155
Redoubt 1990	Andesite	24-32	Plag	64.5-66	4	2228-2238	1.6×10^4-1.8×10^4	840-950	100
Krakatau 1883	Basalt	0-10 [b]	Plag [b]	61.6	sat. [b]	2355-2363	24-31	984-1011	100-150
Minoan – scenario 1	Mafic	22-40	Plag (0.8) CPx (0.2)	61-63	sat. [b]	2157-2167	6.1×10^3-6.7×10^3	880	50
Minoan – scenario 2	Rhyodacite	10-20	Plag	73.5-74	5-6	2213-2173	1.7×10^4-1.4×10^5	845-860	200-250
SW Trident 1953	Andesite	28-43	Plag	74-63	3.5	2150-2295	8.3×10^2-10^4	990-1010	90

Dutton 1989	Mafic recharge	10-30	Plag	74	sat.	2546-2556	80-88	1080-1180	200 [b]
Pinatubo 1991	Basalt	19-25	Plag (0.75) Hb+Aug+Ol (0.25)	73.2	2-3 usat.	2159-2169	6.1×10^2-6.7×10^2	1250	250
Usu 1663	Mafic	0-1	Plag	54	n.u.	2351-2364	57-98	1000-1050	n.u.

[a] Calculated from bulk values given in the reference(s).

[b] Assumed value.

Supplementary references:

Barclay, J., Rutherford, M.J., Carroll, M.R., Murphy, M.D., Devine, J.D., Gardner, J., Sparks, R.S.J., 1998. Experimental phase equilibria constraints on pre-eruptive storage conditions of the Soufriere Hills magma. Geophys. Res. Lett. 25, 3437–3440.

Benyahia, S., Syamlal, M., O'Brien, T.J., 2012. Summary of MFIX equations 2012-1. URL Httpsmfix Netl Doe GovdocumentationMFIXEquations2012-1 Pdf.

Bernard, A., Knittel, U., Weber, B., Weis, D., Albrecht, A., Hattori, K., Klein, J., Oles, D., 1996. Petrology and geochemistry of the 1991 eruption products of Mount Pinatubo (Luzon, Philippines) 1126.

Browne, B.L., Eichelberger, J.C., Patino, L.C., Vogel, T.A., Dehn, J., Uto, K., Hoshizumi, H., 2006. Generation of Porphyritic and Equigranular Mafic Enclaves During Magma Recharge Events at Unzen Volcano, Japan. J. Petrol. 47, 301–328. https://doi.org/10.1093/petrology/egi076

Cadoux, A., Scaillet, B., Druitt, T.H., Deloule, E., 2014. Magma Storage Conditions of Large Plinian Eruptions of Santorini Volcano (Greece). J. Petrol. 55, 1129–1171. https://doi.org/10.1093/petrology/egu021

Camus, G., Gourgaud, A., Vincent, P.M., 1987. Petrologic evolution of Krakatau (Indonesia): Implications for a future activity. J. Volcanol. Geotherm. Res. 33, 299–316. https://doi.org/10.1016/0377-0273(87)90020-5

Cioni, R., Civetta, L., Marianelli, P., Metrich, N., Santacroce, R., Sbrana, A., 1995. Compositional layering and syn-eruptive mixing of a periodically refilled shallow magma chamber: the AD 79 Plinian eruption of Vesuvius. J. Petrol. 36, 739–776.

Coombs, M.L., Eichelbeger, J.C., Rutherford, M.J., 2000. Magma storage and mixing conditions for the 1953-74 eruptions of Southwest Trident volcano, Katmai National Park, Alaska. Contrib. Mineral. Petrlogy 140, 99–118.

Coombs, M.L., Eichelberger, J.C., Rutherford, M.J., 2002. Experimental and textural constraints on mafic enclave formation in volcanic rocks. J. Volcanol. Geotherm. Res. 119, 125–144.

Coombs, M.L., Gardner, J.E., 2001. Shallow-storage conditions for the rhyolite of the 1912 eruption at Novarupta, Alaska. Geology 29, 775–778.

Cottrell, E., Gardner, J.E., Rutherford, M.J., 1999. Petrologic and experimental evidence for the movement and heating of the pre-eruptive Minoan rhyodacite (Santorini, Greece). Contrib. Mineral. Petrol. 135, 315–331.

Couch, S., Sparks, R.S.J., Carroll, M.R., 2001. Mineral disequilibrium in lavas explained by convective self-mixing in open magma chambers. Nature 411, 1037–1039.

Cui, X., Li, J., Chan, A., Chapman, D., 2014. Coupled DEM–LBM simulation of internal fluidisation induced by a leaking pipe. Powder Technol. 254, 299–306. https://doi.org/10.1016/j.powtec.2014.01.048

Druitt, T.H., 2014. New insights into the initiation and venting of the Bronze-Age eruption of Santorini (Greece), from component analysis. Bull. Volcanol. 76, 794. https://doi.org/10.1007/s00445-014-0794-x

Druitt, T.H., Edwards, L., Mellors, R.M., Pyle, D.M., Sparks, R.S.J., Lanphere, M., Davies, M., Barreirio, B., 1999. Santorini Volcano. Geol. Soc. Mem. 19, 165.

Eichelberger, J.C., Izbekov, P.E., 2000. Eruption of andesite triggered by dyke injection: contrasting cases at Karymsky Volcano, Kamchatka and Mt Katmai, Alaska. Philos. Trans. RS Lond. A358, 1465–1485.

Ergun, S., 1952. Fluid flow through packed columns. Chem Eng Prog 48, 89–94.

Flaherty, T., Druitt, T.H., Tuffen, H., Higgins, M.D., Costa, F., Cadoux, A., 2018. Multiple timescale constraints for high-flux magma chamber assembly prior to the Late Bronze Age eruption of Santorini (Greece). Contrib. Mineral. Petrol. 173, 75. https://doi.org/10.1007/s00410-018-1490-1

Garg, R., Galvin, J., Li, T., Pannala, S., 2010. Documentation of open-source MFIX–DEM software for gas-solids flows. URL Httpsmfix Netl Doe Govdocumentationdemdoc2012-1 PdfAccessed 31 March 2014.

Gidaspow, D., 1986. Hydrodynamics of Fiuidizatlon and Heat Transfer: Supercomputer Modeling. Appl. Mech. Rev. 39, 1–23. https://doi.org/10.1115/1.3143702

Hammer, J.E., Rutherford, M.J., Hildreth, W., 2002. Magma storage prior to the 1912 eruption at Novarupta, Alaska. Contrib. Mineral. Petrol. 144, 144–162.

Holtz, F., Sato, H., Lewis, J., Behrens, H., Nakada, S., 2005. Experimental petrology of the 1991-1995 Unzen dacite, Japan. Part I. Phase relations, phase composition and pre-eruptive conditions. J. Petrol. 46, 319–337.

Humphreys, M.C.S., Edmonds, M., Christopher, T., Hards, V., 2010. Magma hybridisation and diffusive exchange recorded in heterogeneous glasses from Soufrière Hills Volcano, Montserrat. Geophys. Res. Lett. 37.

Izbekov, P., Gardner, J.E., Eichelberger, J.C., 2004. Comagmatic granophyre and dacite from Karymsky volcanic center, Kamchatka: experimental constraints for magma storage conditions. J. Volcanol. Geotherm. Res. 131, 1–18.

Izbekov, P.E., Eichelberger, J.C., Patino, L.C., Vogel, T.A., Ivanov, B.V., 2002. Calcic cores of plagioclase phenocrysts in andesite from Karymsky volcano: Evidence for rapid introduction by basaltic replenishment. Geology 30, 799–802. https://doi.org/10.1130/0091-7613(2002)030<0799:CCOPPI>2.0.CO;2

Kilgour, G., Blundy, J., Cashman, K., Mader, H.M., 2013. Small volume andesite magmas and melt–mush interactions at Ruapehu, New Zealand: evidence from melt inclusions. Contrib. Mineral. Petrol. 166, 371–392. https://doi.org/10.1007/s00410-013-0880-7

Mandeville, C.W., Carey, S., Sigurdsson, H., 1996. Magma mixing, fractional crystallization and volatile degassing during the 1883 eruption of Krakatau volcano, Indonesia. J. Volcanol. Geotherm. Res. 74, 243–274.

Miller, T.P., Chertkoff, D.G., Eichelberger, J.C., Coombs, M.L., 1999. Mount Dutton volcano, Alaska: Aleutian arc analog to Unzen volcano, Japan. J. Volcanol. Geotherm. Res. 89, 275–301.

Murphy, M.D., Sparks, R.S.J., Barclay, J., Carroll, M.R., Brewer, T.S., 2000. Remobilization of andesite magma by intrusion of mafic magma at the Soufriere Hills Volcano, Montserrat, West Indies. J. Petrol. 41, 21–42.

Nakagawa, M., Wada, K., Thordarson, T., Wood, C.P., Gamble, J.A., 1999. Petrologic investigations of the 1995 and 1996 eruptions of Ruapehu volcano, New Zealand: formation of discrete and small magma pockets and their intermittent discharge. Bull. Volcanol. 61, 15–31.

Nakagawa, M., Wada, K., Wood, C.P., 2002. Mixed magmas, mush chambers and eruption triggers: Evidence from zoned clinopyroxene phenocrysts in andesitic scoria from the 1995 eruptions of Ruapehu volcano, New Zealand. J. Petrol. 43, 2279–2303.

Nye, C.J., Swanson, S.E., Avery, V.F., Miller, T.P., 1994. Geochemistry of the 1989-1990 eruption of Redoubt volcano: Part I. Whole-rock major- and trace-element chemistry. J. Volcanol. Geotherm. Res. 62, 429–452.

Pallister, J.S., Hoblitt, R.P., Meeker, G.P., Knight, R.J., Siems, D.F., 1996. Magma mixing at Mount Pinatubo: petrographic and chemical evidence from the 1991 deposits. pp. 687–731.

Pallister, J.S., Hoblitt, R.P., Reyes, A.G., 1992. A basalt trigger for the 1991 eruptions of Pinatubo volcano ? Nature 356, 426–428.

Pichavant, M., Poussineau, S., Lesne, P., Solaro, C., Bourdier, J.-L., 2018. Experimental Parametrization of Magma Mixing: Application to the ad 1530 Eruption of La Soufrière, Guadeloupe (Lesser Antilles). J. Petrol. 59, 257–282. https://doi.org/10.1093/petrology/egy030

Plail, M., Edmonds, M., Woods, A.W., Barclay, J., Humphreys, M.C.S., Herd, R.A., Christopher, T., 2018. Mafic enclaves record syn-eruptive basalt intrusion and mixing. Earth Planet. Sci. Lett. 484, 30–40. https://doi.org/10.1016/j.epsl.2017.11.033

Scaillet, B., Pichavant, M., Cioni, R., 2008. Upward migration of Vesuvius magma chamber over the past 20,000 years. Nature 455, 216–220.

Self, S., 1992. Krakatau revisited: The course of events and interpretation of the 1883 eruption. GeoJournal 28, 109–121. https://doi.org/10.1007/BF00177223

Shi, Y.F., Yu, Y.S., Fan, L.T., 1984. Incipient fluidization condition for a tapered fluidized bed. 484–489.

Singer, B.S., Costa, F., Herrin, J.S., Hildreth, W., Fierstein, J., 2016. The timing of compositionally-zoned magma reservoirs and mafic 'priming' weeks before the 1912 Novarupta-Katmai rhyolite eruption. Earth Planet. Sci. Lett. 451, 125–137. https://doi.org/10.1016/j.epsl.2016.07.015

Swanson, S.E., Nye, C.J., Miller, T.P., Avery, V.F., 1994. Geochemistry of the 1989-1990 eruption of Redoubt volcano: Part II. Evidence from mineral and glass chemistry. J. Volcanol. Geotherm. Res. 62, 453–468.

Syamlal, M., Rogers, W., OBrien, T.J., 1993. MFIX documentation theory guide. USDOE Morgantown Energy Technology Center, WV (United States).

Takahashi, R., Nakagawa, M., 2013. Formation of a Compositionally Reverse Zoned Magma Chamber: Petrology of the ad 1640 and 1694 Eruptions of Hokkaido-Komagatake Volcano, Japan. J. Petrol. 54, 815–838. https://doi.org/10.1093/petrology/egs087

Tomiya, A., Takahashi, E., 2005. Evolution of the Magma Chamber beneath Usu Volcano since 1663: a Natural Laboratory for Observing Changing Phenocryst Compositions and Textures. J. Petrol. 46, 2395–2426. https://doi.org/10.1093/petrology/egi057

Vetere, F., Behrens, H., Schuessler, J.A., Holtz, F., Misiti, V., Borchers, L., 2008. Viscosity of andesite melts and its implication for magma mixing prior to Unzen 1991–1995 eruption. J. Volcanol. Geotherm. Res., Scientific drilling at Mount Unzen 175, 208–217. https://doi.org/10.1016/j.jvolgeores.2008.03.028

Wolf, K.J., Eichelbeger, J.C., 1997. Syneruptive mixing, degassing, and crystallization at Redoubt Vocano, eruption of December, 1989 to May 1990. J. Volcanol. Geotherm. Res. 75, 19–37.